CCAM: China Catchment Attributes and Meteorology dataset

Zhen Hao[2, *], Jin Jin[1,2, *], Runliang Xia[2], Shimin Tian[2], Wushuang Yang[2], Qixing Liu[2], Min Zhu[2], Tao Ma[2], Chengran Jing[2], Yanning Zhang[1]

[1] School of Computer Science, Northwestern Polytechnical University, Xi'an, China, 710072
[2] Yellow River Institute of Hydraulic Research, Zhengzhou, China, 450003
*These authors contributed equally to this work.

Correspondence to: Jin Jin (jinjinhao@21cn.com)

Abstract. The absence of a compiled large-scale catchment characteristics dataset is a key obstacle limiting the development of large sample hydrology research in China. We introduce the first large-scale catchment attribute dataset in China. We compiled diverse data sources, including soil, land cover, climate, topography, and geology, to develop the dataset. The dataset also includes catchment-scale 31-year meteorological time series from 1990 to 2020 for each basin. Potential evapotranspiration time series based on Penman's equation are derived for each basin. The 4,911 catchments included in the dataset cover all of China. We introduced several new indicators that describe the catchment geography and the underlying surface differently from previously proposed datasets. The resulting dataset has a total of 125 catchment attributes and includes a separate HydroMLYR dataset containing standardized weekly averaged streamflow for 102 basins in the Yellow River Basin. The standardized streamflow data should be able to support machine learning hydrology research in the Yellow River Basin. The dataset is freely available at http://doi.org/10.5281/zenodo.5137288. In addition, the accompanying code used to generate the dataset is freely available at https://github.com/haozhen315/CCAM-China-Catchment-Attributes-and-Meteorology-dataset and supports the generation of catchment characteristics for any custom basin boundaries. Compiled data for the 4,911 basins covering all of China and the open source code should be able to support the study of any selected basins rather than being limited to only a few basins.

1 Introduction

Rainfall, interception, evaporation and evapotranspiration, groundwater flow, subsurface flow and surface runoff are the main components of the terrestrial hydrological cycle. These processes are affected by the nature of the catchment, such as the ability of the soil to hold water. Catchment attributes influence water movement and the storage of the catchment such that hydrologic behaviors can vary across catchments (Van Werkhoven et al., 2008). Studying a large set of terrestrial catchments often provides insights that cannot be obtained when looking at individual cases or small sets (Coron et al., 2012; Kollat et al., 2012a; Newman et al., 2015; Lane et al., 2019). For example, a calibrated model may not be applicable in a watershed with vastly different properties. However, by examining a large sample of catchments, it is possible for a data-driven model to learn the similarities and differences among hydrological behaviors across catchments (Kratzert et al., 2019). Prediction in ungauged

basins presents a challenging problem in hydrology. The central challenge is how to extrapolate hydrologic information from gauged to ungauged basins, and solving this problem is contingent on understanding the similarities and differences between different catchments. Regionally and temporally imbalanced observations increase the difficulty of the problem. For a model to successfully simulate the ungauged areas, it must adapt itself to the varying hydrologic behaviors present in different catchments. Kratzert et al. (2019) show that encoding catchment characteristics (e.g., soil characteristics, land cover, topography) into a data-driven model can guide the model to behave differently in response to the meteorological time series input based on different sets of catchment attributes.

Large sample hydrological datasets are the foundation of many hydrological studies (Silberstein, 2006; Shen et al., 2018; Nevo et al., 2019). The term "big hydrologic data" refers to all data influencing the water cycle, such as the meteorological variables, infiltration characteristics of the study area, land use or land cover types, physical and geological features of the study catchment, etc. Many studies are based on large-scale hydrologic data (Coron et al., 2012; Singh et al., 2014b; Berghuijs et al., 2017; Gudmundsson et al., 2019; Tyralis et al., 2019). Basin-oriented datasets are of great significance in hydrological research. For example, comparative hydrology (De Araújo and González Piedra, 2009; Singh et al., 2014a) focuses on understanding how hydrological processes interact with the ecosystem—in particular, how hydrologic behaviors change in response to changes in the surface and subsurface of the earth to determine to what extent hydrological predictions can be transferred from one area to another. Large-sample catchment attribute datasets provide opportunities to research interrelationships among catchment attributes. Seybold et al. (2017) study the correlations between river junction angles and geometric factors, downstream concavity, and aridity. Oudin et al. (2008) investigate the link between land cover and mean annual streamflow based on 1,508 basins representing a large hydroclimatic variety. Voepel et al. (2011) examine how the interaction of climate and topography influences vegetation response.

Worldwide data sharing has become a trend (Wickel et al., 2007; Ceola et al., 2015; Blume et al., 2018; Wang et al., 2020), and the amounts of hydrologic data available are ever increasing. However, these data typically come from different providers and are compiled in various formats. ASTGTM (Abrams et al., 2020) provides a global digital elevation model; GliM (Hartmann and Moosdorf, 2012) includes rock type data globally; MODIS provides data products (Didan, 2015; Knyazikhin, 1999; Myneni et al., 2015; Running et al., 2017; Sulla-Menashe and Friedl, 2018) that describe features of the land and the atmosphere derived from remote sensing observations; Yamazaki et al. (2019) provide a global flow direction map at three arc-second resolution; HydroBASINS (Lehner, 2014) provides basin boundaries at different scales globally; GDBD (Masutomi et al., 2009) provides basin boundaries with geographic attributes; GLHYMPS (Gleeson et al., 2014) provides a global map of subsurface permeability and porosity; and the SoilGrids250 m (Hengl et al., 2017) dataset provides global numeric soil properties. Local government agencies often hold meteorological data such as precipitation and evaporation, and the amount of these data is also growing.

However, the data mentioned above are rarely spatially aggregated to the catchment scale, making it difficult for researchers to use them. Properly preprocessed and formatted datasets are of great importance in hydrology research. Searching for appropriate data sources, preprocessing, and formatting often consume considerable time. In some cases, individual research groups either do not know where to obtain the appropriate data or cannot properly process the data into the desired format. In summary, although data sharing is being advocated in the community, it is usually difficult for the public to obtain the required data, either because there are insufficient observations or because of the difficulties associated with data processing.

Recently, there have been efforts (Addor et al., 2017; Alvarez-Garreton et al., 2018; Chagas et al., 2020; Coxon et al., 2020) to compile different types of data sources to form large-scale hydrological datasets. These four collected datasets cover the continental United States, Chile, Brazil, and Great Britain. Addor et al. (2020) review these datasets and discuss the guidelines for producing large-sample hydrological datasets and the limitations of the currently proposed datasets. The static properties of 671 river basins in the United States are calculated by CAMELS (Addor et al., 2017), which is an extension of a previously proposed hydrometeorological dataset (Newman et al., 2015). Unfortunately, it is impossible to publish streamflow data in China at present. The CAMELS dataset has been used to support much research. For example, Knoben et al. (2019) compare metrics used in hydrology based on simulations in many basins. Tyralis et al. (2019) study the relationship between shape parameters and basin attributes based on a sizeable basin-oriented dataset.

There is currently no compilation of China-specific catchment attribute datasets. An alternative—the HydroATLAS (Linke et al., 2019) dataset, which is on a global scale—basically performs zonal statistics on the source data. HydroATLAS lacks many indicators that make derivations from source data, such as rainfall seasonality, the proportion of precipitation falling as snow, basin shape factors and root depth distributions. Moreover, the meteorological data are only up to the year 2000, which is outdated.

In summary, a lack of a compiled catchment attribute dataset is a key obstacle limiting the development of large-sample hydrology research in China. Inspired by (Addor et al., 2017), we compiled multiple data sources, including basin topography, climate indices, land cover characteristics, soil characteristics and geological characteristics. Unlike (Addor et al., 2017), the catchments included in the dataset cover the entire study area instead of being limited to a few data sources.

The proposed dataset is the first dataset that provides catchment meteorological time series and catchment attributes of China. We compiled and named the dataset following most standards set by the previously proposed datasets. The dataset consists of all derived basin boundaries from the Digital Elevation Model (DEM), which is a subset of the Global Drainage Basin Dataset (Masutomi et al., 2009). The Global Drainage Basin Dataset (GDBD) is derived at high resolution (100 m-1 km) and has good geographic agreement with existing global drainage basin data in China. In addition, previously proposed datasets (Addor et

al., 2017; Alvarez-Garreton et al., 2018; Chagas et al., 2020; Coxon et al., 2020) report only the most frequent catchment land cover and lithology types. By contrast, CCAM calculates the proportions of all land cover and lithology types.

In addition to the basinwise attributes provided in CCAM, we propose HydroMLYR, a hydrology dataset for machine learning research in the Yellow River Basin providing weekly averaged standardized streamflow data for 102 basins in the Yellow River Basin (YRB). HydroMLYR is proposed to support machine learning hydrology research in the YRB. Traditional hydrological models face long-standing challenges, such as their inability to capture hydrological process mechanism complexity (Kollat et al., 2012b), which is due to the structural limitations of the conceptual models. Data-driven strategies represented by machine learning are proposed to overcome some existing obstacles, and these strategies offer a new way for researchers to acquire knowledge capable of transforming the research pattern from hypothesis-driven to data-driven. Feng et al. (2020) propose a flexible data integration fusing various types of observations to improve rainfall-runoff modeling. Their research shows that combining different data resources improves predictions in regions with high autocorrelation in streamflow. Wongso et al. (2020) develop a model predicting the state-level per capita water use in the United States, taking various geographic, climatic, and socioeconomic variables as input. Their research also identifies key factors associated with high water usage. Mei et al. (2020) propose a statistical framework for spatial downscaling to obtain hyperresolution precipitation data. Their results show improvements compared with the original product. Brodeur et al. (2020) apply machine learning techniques—namely, bootstrap aggregation and cross-validation—to reduce overfitting in reservoir control policy search. Ni and Benson (2020) propose an unsupervised machine learning method to differentiate flow regimes and identify capillary heterogeneity trapping and show the promise of machine learning methods for analyzing large datasets from coreflooding experiments. Legasa and Gutiérrez (2020) propose applying a Bayesian network for multisite precipitation occurrence generation, and the proposed methodology shows improvements over existing methods. The proposed dataset can be used to develop or verify machine learning models in the YRB.

This paper is organized as follows. Section 2 describes the study area. Sections 3–7 describe the five classes of computed catchment attributes. Section 8 describes the proposed catchment-scale meteorological time series. Section 9 introduces the HydroMLYR dataset. Section 10 describes the code and data availability. Section 11 is our concluding remarks.

2 Study area

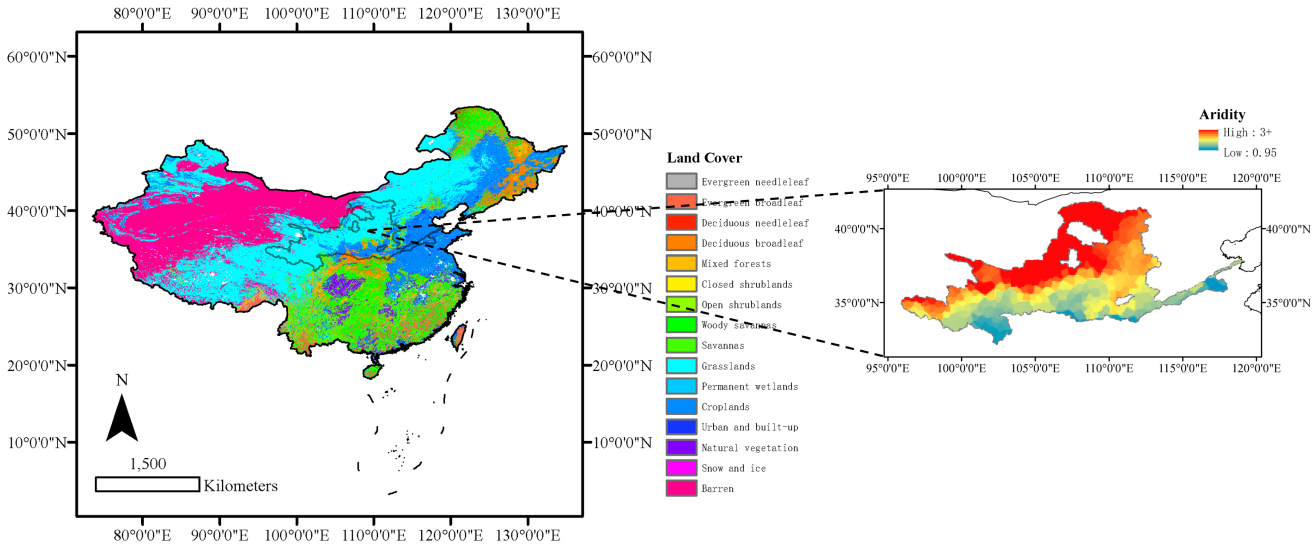

Figure 1: Left: Study area of CCAM and the distribution of land cover types. The studied basins cover the whole of China. Right: Study area of HydroMLYR and the distribution of aridity (PET/P) index. YRB is a generally arid area. The dataset provided can be used as a good sample for studying hydrology in arid regions.

The study area corresponds to the whole of China (Fig. 1), which is characterized by diverse climate and terrain characteristics and spans from 18.2° N to 52.3° N and 76.0° E to 134.3° E. Mountains, plateaus, and hills account for approximately two-thirds of the area of China, and the remaining areas are basins and plains. China's topography is similar to a three-level ladder in that it is high in the west and low in the east. The Qinghai-Tibet Plateau, which is located in western China and is the highest plateau globally with a mean elevation of over 4,000 meters, is the first step of China's topography. The Xinjiang region, the Loess Plateau, the Sichuan Basin, and the Yunnan-Guizhou Plateau to the north and east are the second steps of China's topography. The mean sea level here is between 1,000 and 2,000 meters. Plains and hills dominate the east of the Daxinganling-Taihang Mountains to the coastline, which comprises the third step of China's topography. The elevation of this step descends to 500-1,000 meters. To better characterize the studied catchments, we derived various attributes. Table 1 compares the number of derived attributes between several proposed datasets.

Table 1: Number of computed attributes in CAMELS, CAMELS-BR and CCAM.

Attribute class	CAMELS(A17)	CAMELS-BR	CCAM
Location and topography	9	11	12
Geology	7	7	18
Soil	11	6	54
Land cover	8	11	22

Climatic indices	11	13	17
Human intervention indices	-	4	2
Total	46	52	125

In China, precipitation and temperature vary significantly throughout China, which forms a diverse climatic environment. According to the Köppen Climate Classification System, moving from northwest to southeast, China's climate gradually evolves from a cold desert (BW_k) climate, a tundra (ET) climate, and a warm and temperate continental (D_{fa} and D_{wb}) climate to a humid subtropical (C_{wa}) climate and warm oceanic (C_{fa}) climate. From the perspective of temperature zones, there are tropical, subtropical, warm temperate, medium temperate, cold temperate and Qinghai-Tibet Plateau regions, and there are humid, semihumid, semiarid, and arid regions from the perspective of wet vs. dry zones. Moreover, the same temperature zone can contain multiple dry and wet zones. Therefore, there may be differences in heat and wetness in the same climate type. The complexity of the terrain makes the climate even more complex and diverse. In addition, China has a wide range of regions which are affected by alternating winter and summer monsoons. Compared with other parts of the world at the same latitude, these areas have lower winter temperatures, higher summer temperatures, significant annual temperature differences, and concentrated precipitation in summer. The cold and dry winter monsoon occurs in Asia's interior, far from the ocean. Winter rainfall in most parts of China is low and accompanied by low temperatures. The summer monsoon is warm and humid and comes from the Pacific and Indian Oceans. Precipitation generally increases during this time. Table 2 compares the provided forcing variables in CAMELS, CAMELS-BR and CCAM.

Table 2: Summary of forcing variables provided in CAMELS, CAMELS-BR and CCAM.

Forcing data class	CAMELS	CAMELS-BR	CCAM
Temperature	Yes	Yes	Yes
Precipitation	Yes	Yes	Yes
Solar radiation	Yes	**No**	Yes
Day length	Yes	**No**	**No**
Sunshine hours	**No**	**No**	Yes
Humidity	Yes	**No**	Yes
Snow water equivalent	Yes	**No**	**No**
Wind velocity	**No**	**No**	Yes
Ground surface pressure	Yes	**No**	Yes
Observed evaporation	**No**	Yes	Yes
Potential evapotranspiration	**No**	Yes	Yes

3 Climatic indices

Raw meteorological data are provided by the China Meteorological Data Network and released as the SURF_CLI_CHN_MUL_DAY (V3.0) dataset, which provides the longest period (1951-2020) of meteorological time series in China. The SURF_CLI_CHN_MUL_DAY product includes site observations of pressure, temperature, relative humidity, precipitation, evaporation, wind speed, sunshine duration, and ground surface temperature (Table 3). The inverse distance weighting method is used to interpolate the site observations. To ensure data quality, we use the latter 31-year record (from 1990 to 2020) to construct the dataset since the site distribution was sparse in the early observations (Fig. 2). We computed more climatic characteristics than most other datasets (Table 2). These variables are useful in hydrological modeling; for example, wind speed can affect actual evapotranspiration. To remain consistent with CAMELS (Addor, Newman et al. 2017), we determined all climatic attributes (Woods, 2009) provided in the CAMELS dataset. As a result, the proposed dataset provides more meteorological variables and a longer time series (1990-2020) than CAMELS and CAMELS-CL. A summary of the derived climate indices is presented in Table A1. The national distributions of the climate indicators are shown in Fig. 3.

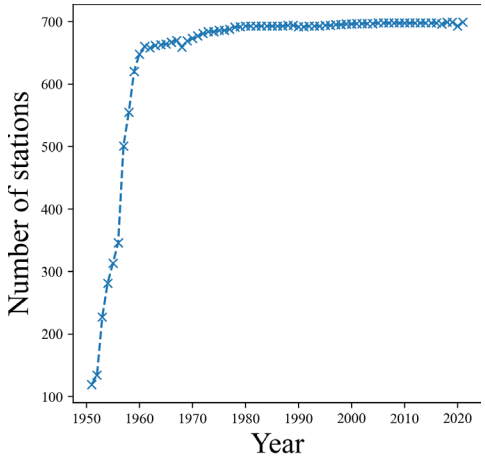

Figure 2: Changes in the number of meteorological stations in China. There were only 119 stations in 1951. This number increased rapidly from 1951 to the early 1960s, and the number of stations remained stable after 2000. To ensure data quality, we used the latter 31-years (from 1990 to 2020) to construct the dataset.

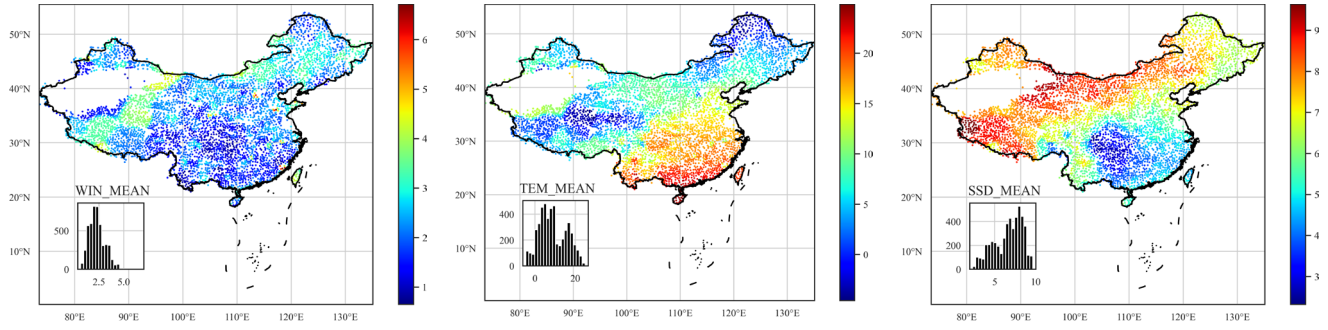

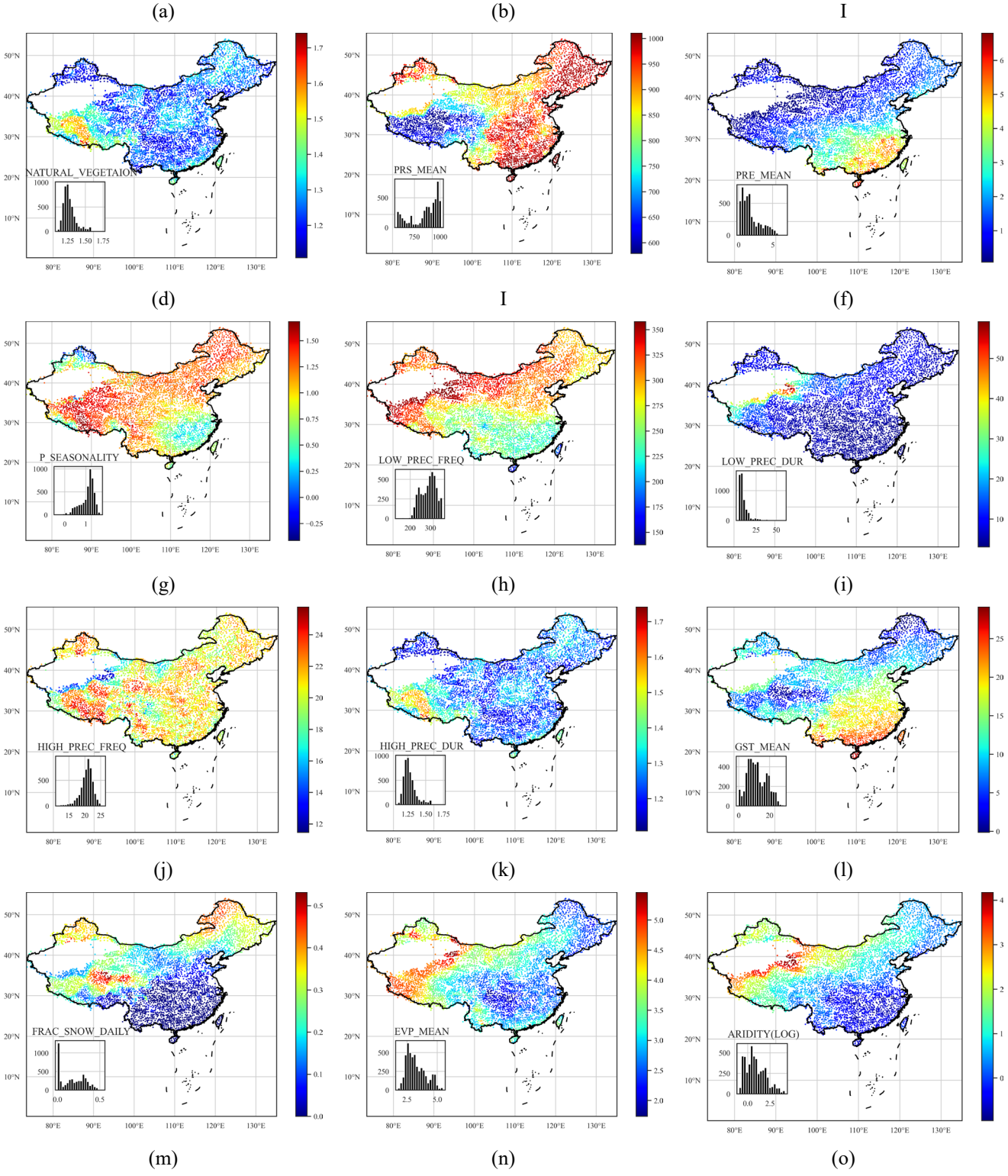
(a)
(b)
I
NATURAL_VEGETAION
PRS_MEAN
PRE_MEAN
(d)
I
(f)
P_SEASONALITY
LOW_PREC_FREQ
LOW_PREC_DUR
(g)
(h)
(i)
HIGH_PREC_FREQ
HIGH_PREC_DUR
GST_MEAN
(j)
(k)
(l)
FRAC_SNOW_DAILY
EVP_MEAN
ARIDITY(LOG)
(m)
(n)
(o)

Figure 3: Distributions of climatic indices over China. All basins are plotted in the same size. When extreme values of a variable affect visualization (causing most areas to have the same color), the log values are used for visualization.

The instruments used to measure potential evaporation were updated from 2000 to 2005. Early observations can be multiplied by a correction coefficient to approximate the new tools. However, the coefficient varies across stations, making the approach infeasible. To complement this, we calculated potential evapotranspiration (PET) based on a modified Penman's equation (Appendix A) and other observed meteorological variables, which provides a series of consistent potential evaporation estimations for reference.

The average daily precipitation in China is highest in the southeast and lowest in the northwest. It is also higher in coastal areas than in interior land. Ground surface pressure is positively correlated with elevation and is highest in the Qinghai-Tibet Plateau and the lowest in the Southeast Plain. The average relative humidity is generally positively correlated with precipitation; it is also higher in some forested areas, such as the Taihang and Daxingan Mountains. The Qinghai-Tibet Plateau has the lowest average temperature, and the southern coastal area has the highest. A distinctive feature of the distribution of wind speed is the high wind speed in mountainous areas. The highest wind speed occurs in the southeast coastal area (> 6 meters per second).

4 Geology

To describe the lithological characteristics of each catchment, we used the same two global datasets as CAMELS: Global Lithological Map (GliM) (Hartmann and Moosdorf, 2012) and Global Hydrogeology MaPS (GLHYMPS) (Gleeson et al., 2014). Figure 4 presents the distributions of the geological types.

GLiM provides a high-resolution global lithological map assembled from existing regional geological maps; it has been widely used to construct datasets (e.g., SoilGrids250 m (Hengl et al., 2017)). However, the data quality of GLiM can vary among spatial locations depending on the quality of the original regional geological maps. GLiM consists of three levels: the first level contains 16 lithological classes, and the additional two levels describe more specific lithological characteristics. The GLiM is represented by 1,235,400 polygons which are converted to raster format for the basin-scale lithological type statistics. For China, the compiled regional data sources (MGC, 1991; BGX, 1992; CGS, 2001) have slightly lower resolutions than the GLiM target resolution (1:1 000 000). However, for a basin-scale study with a mean basin area of over 2,000 km^2, the classification accuracy should satisfy most applications. In contrast to CAMELS and CAMELS-CL, we determined each lithological class's contribution to the catchment instead of recoding the first and second most frequent classes only.

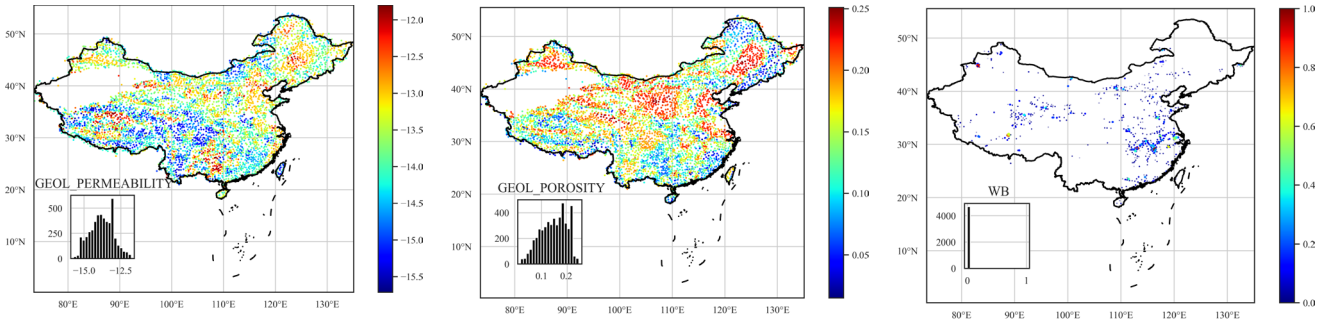

(a) (b) (c)

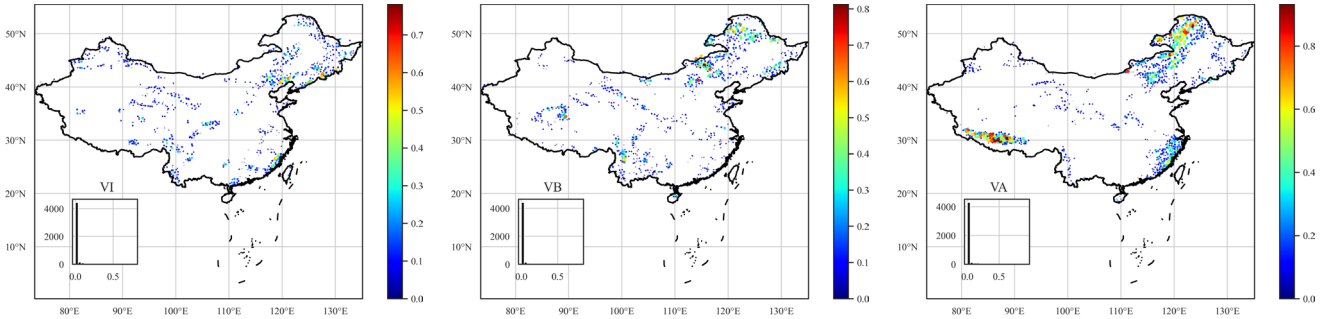

(a) (b) (c)

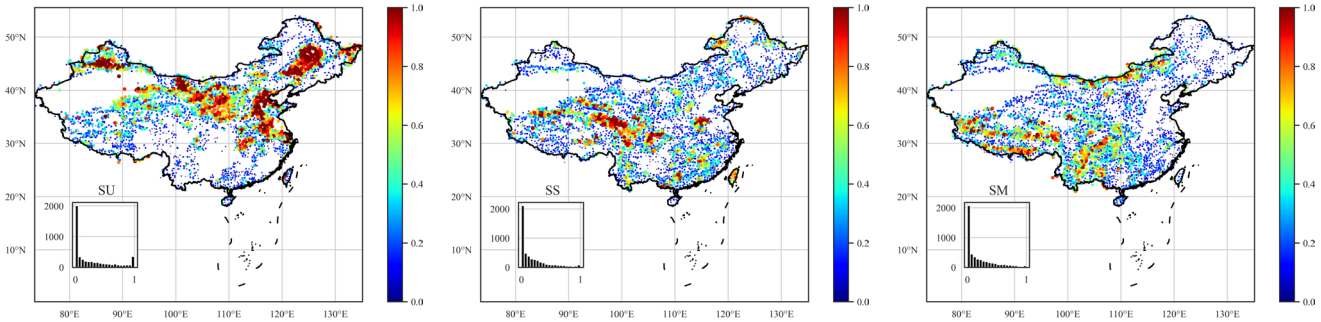

(d) (e) (f)

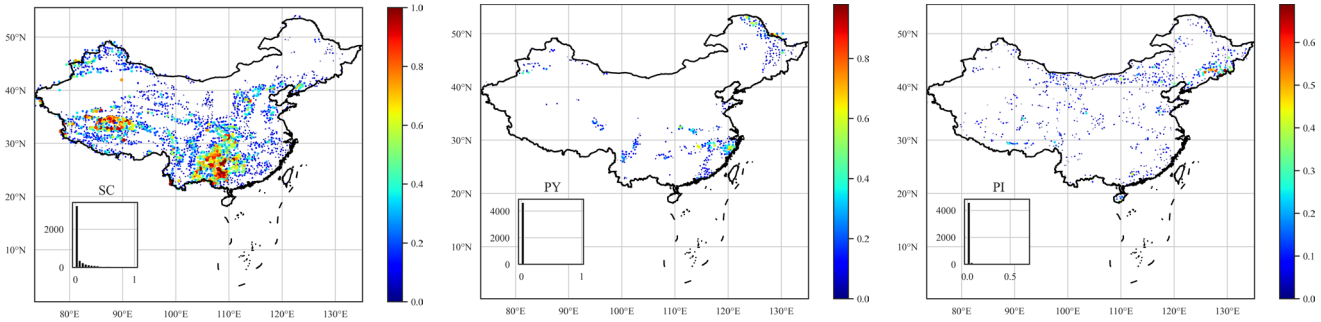

(g) (h) (i)

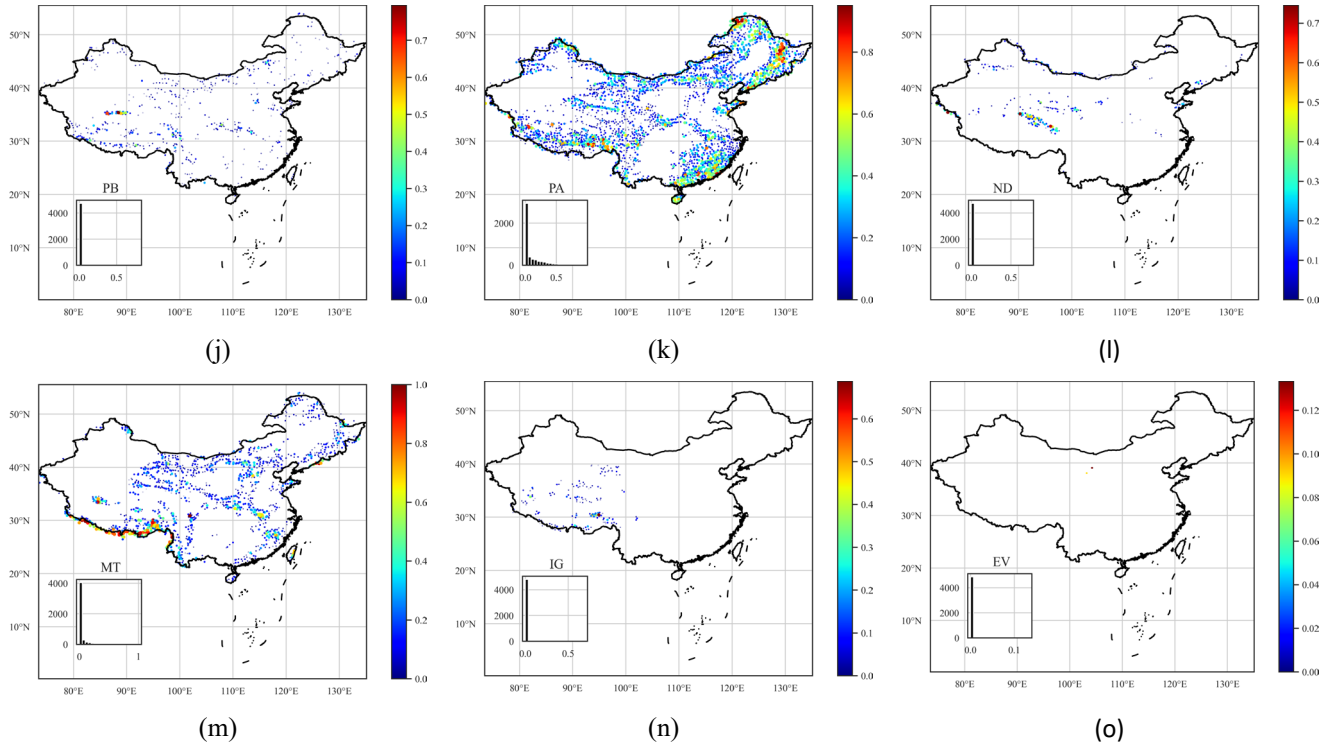

Figure 4: Distributions of geological characteristics throughout China. For lithologies, the plot size is scaled by the lithology proportion.

GLobal HYdrogeology MaPS (GLHYMPS) provides a global estimation of subsurface permeability and porosity, two critical characteristics for soil hydrological classification. Porosity and permeability influence an area's infiltration capacity. Soil with high porosity is likely to contain more water, and highly permeable soil transmits water relatively quickly. Based on the high-resolution map of GLiM, which can differentiate fine- and coarse-grained sediments and sedimentary rocks, GLHYMPS determines subsurface permeability depending on the different permeabilities of rock types. For the proposed dataset, we calculated the catchment arithmetic mean for porosity. Following (Gleeson et al., 2011), the logarithmic scale geometric mean is used to represent the subsurface permeability. A summary of the geological characteristics is presented in Table A1.

Porosity and permeability have distributions similar to those of the geological classes. These two characteristics are highly dependent on rock properties; unconsolidated sediments, mixed sedimentary rocks, siliciclastic sedimentary rocks, carbonate sedimentary rocks, and acid plutonic rocks are the five most common geological classes in China. Unconsolidated sediment is the most common rock type in China as it is dominant in 31.9% of catchments and extends from Xinjiang inland to the northeast and the coastal area surrounding the Bohai Sea. Due to the high proportion of unconsolidated sediments present in the rock, these areas typically have high permeability and medium porosity. Mixed sedimentary rocks are the second most common rock type in China, accounting for 20.3% of catchments, and they are predominant in the southern Qinghai-Tibet Plateau, western Yunnan-Guizhou Plateau, and northern Inner Mongolia. These areas typically have high porosity and low

permeability. Siliciclastic sedimentary rocks are found in 17.7% of basins and are mainly distributed in the northern part of the Qinghai-Tibet Plateau and the junction of the Qinghai-Tibet and the Yunnan-Guizhou Plateaus; there are also observations in the eastern inland region. These areas have low subsurface permeability and high subsurface porosity. Among all catchments, 9.8% are dominated by carbonate sedimentary rocks, which are mainly located in eastern Yunnan and the northern Qinghai-Tibet Plateau. Acid plutonic rocks are typically distributed in the mountains surrounding the inland northeast—namely, Daxinganling Mountain and the hills in southern Guangdong and southwestern Guangxi. They are also distributed along the Brahmiputra River in the southern part of the Qinghai-Tibet Plateau. The distribution of acid plutonic rocks is relatively scattered; there are many isolated acid plutonic rock distributions throughout in China which are characterized by medium permeability and high porosity.

The types of rocks in China are dominated by unconsolidated sediments and mixed sedimentary rocks. In 33.86% of the catchments, the dominant rock types occupy less than 50% of the catchment areas, and only 16.8% of basins have a dominant rock type with an area proportion greater than 90%. Among 4,911 basins, 9.4% have prevalent rock types that occupy the area.

5 Landcover

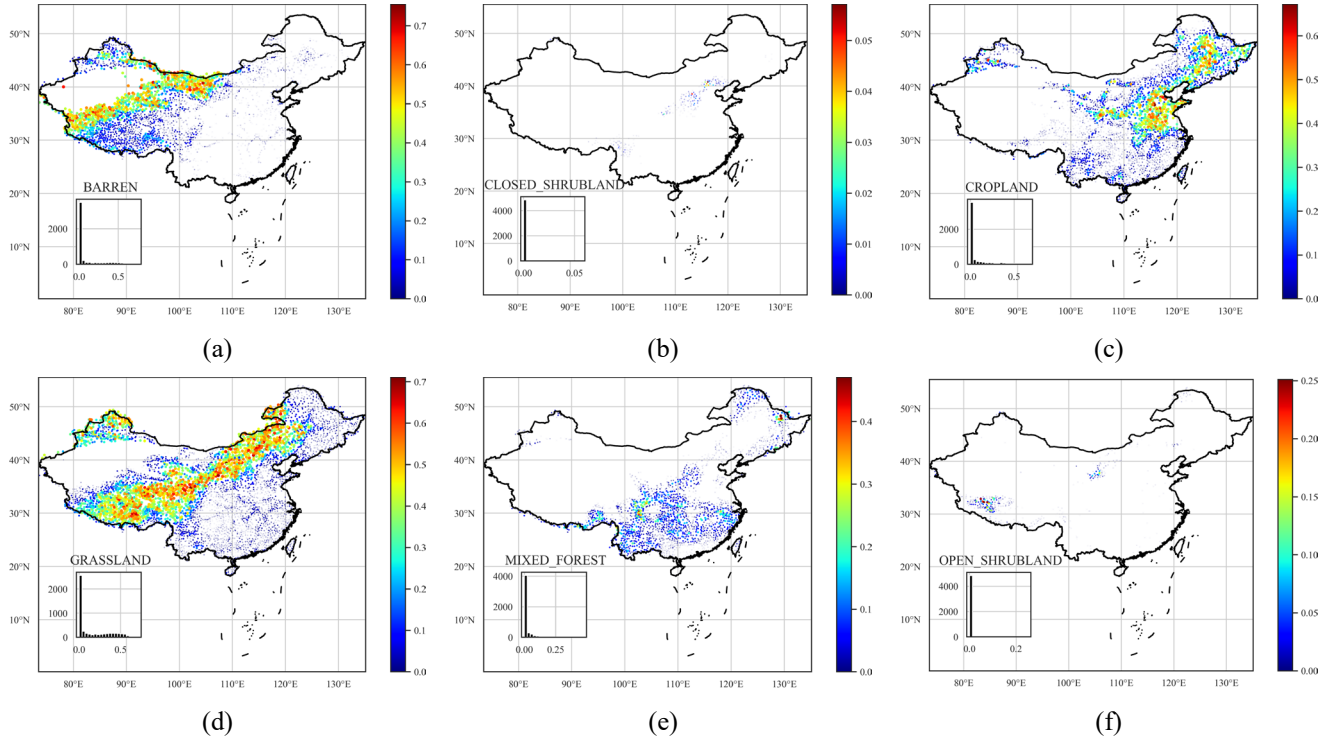

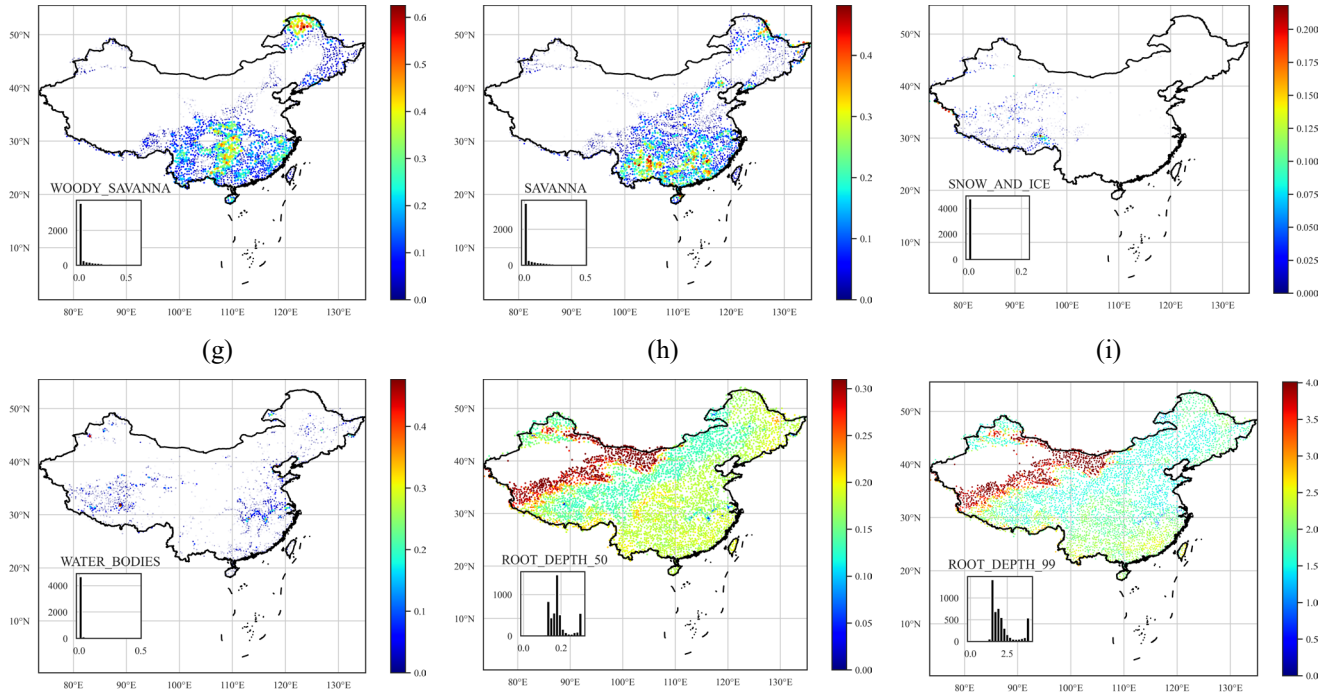

Figure 5: Distributions of land cover characteristics throughout China. For land cover types, the plot size is scaled by the size of the land cover proportion.

We selected two indicators to characterize surface vegetation density and growth: the normalized difference vegetation index (NDVI) and the leaf area index (LAI). NDVI is an indicator with a valid range of -0.2 to 1 that assesses whether the area being observed contains live green vegetation and the plants' overall health. However, NDVI is only a qualitative measurement of vegetation density and cannot provide a quantitative estimate of the vegetation density in the area. Moreover, NDVI often provides inaccurate vegetation density measurements, and only long-term measurements and comparisons can ensure its accuracy. NDVI alone is not enough to estimate the state of the vegetation in an area. Therefore, we selected another indicator, LAI, to supplement the deficiencies of NDVI.

LAI is defined as the total needle surface area per unit of ground area and half of the entire needle surface area per unit of ground surface area. It is a quantifiable value that is functionally related to many hydrological processes, such as water interception (Van Wijk and Williams, 2005). Buermann et al. (2001) verify the validity of the LAI for characterizing vegetation growth. The data sources used are the Terra Moderate Resolution Imaging Spectroradiometer (MODIS) Vegetation Indices (Didan, 2015) for NDVI and the Moderate Resolution Imaging Spectroradiometer (MODIS) (Myneni et al., 2015) for LAI. Following (Addor et al., 2017), we determined the maximum monthly LAI as an indicator that characterizes the vegetation interception capacity, the maximum evaporative capacity and the difference between the maximum and minimum monthly LAI, which represents the LAI's temporal variations.

Land cover classification refers to segmenting the ground into different categories based on remote sensing images. The Terra and Aqua combined Moderate Resolution Imaging Spectroradiometer (MODIS) land cover type provides different results depending on the classification system used. The Annual International Geosphere-Biosphere Programme (IGBP) classification is used to build the dataset, which is derived by the c4.5 decision tree algorithm. The IGBP classification system was formulated by the IGBP Land Cover Working Group in 1995, resulting in 17 categories of land cover types (Belward et al., 1999). Friedl et al. (2010) compare the IGBP data of MODIS with other reference datasets and conclude that the MODIS classification of IGBP has an accuracy of 75%. We determined the fraction of each land cover class for each basin based on the Terra and Aqua combined Moderate Resolution Imaging Spectroradiometer (MODIS) land cover type (Sulla-Menashe and Friedl 2018), which differentiates our dataset from CAMELS and CAMELS-CL (which only calculate the proportion of the dominant types).

Following (Addor et al., 2017), we computed the average rooting depth (50% and 90%) for each catchment based on the IGBP classification using a two-parameter method (Zeng, 2001). The root depth distribution of vegetation affects the ground water holding capacity and the topsoil layer's annual evapotranspiration (Desborough, 1997). Many models use root depth as an essential parameter to characterize soil moisture absorption capacity. Zeng (2001) developed a two-parameter asymptotic equation to estimate root depth distribution, which is global and derived from the IGBP classification to avoid the problem of significantly different root distributions in various research efforts. Figure 5(g) shows root depth distributions of different vegetation types based on (Zeng, 2001). The 90% root depth is usually considered to be "rooting depth;" among the 17 categories of IGBP, cropland has the smallest rooting depth, and open shrubland has the largest. The 90% root depth of all vegetation is less than 2 meters. The national distribution of catchment soil characteristics is shown in Fig. 5.

6 Location and topography

The catchment boundary files are obtained from the global drainage basin dataset (Masutomi et al., 2009). The GDBD dataset was derived from digital elevation models (DEMs) with a high resolution (100 m-1 km), and the errors were corrected by either automatic methods or manually. Additionally, GDBD also provides population and population density estimates for catchments, and these two indicators are also included in our dataset as a measure of human intervention. Global Runoff Data Centre[1] discharge gauging stations were used to reference the derived basins. GDBD has a high average match area rate (AMAR) and good geographic agreement with existing global drainage basin data in China. Precise geographic and topographic information can be derived from the high-quality dataset.

[1] https://www.bafg.de/GRDC/EN/01_GRDC/grdc_node.html

The topography attributes of each catchment are determined by the ASTGTM product retrieved from https://lpdaac.usgs.gov and maintained by the NASA EOSDIS Land Processes Distributed Active Archive Center (LP DAAC) at the USGS Earth Resources Observation and Science (EROS) Center.

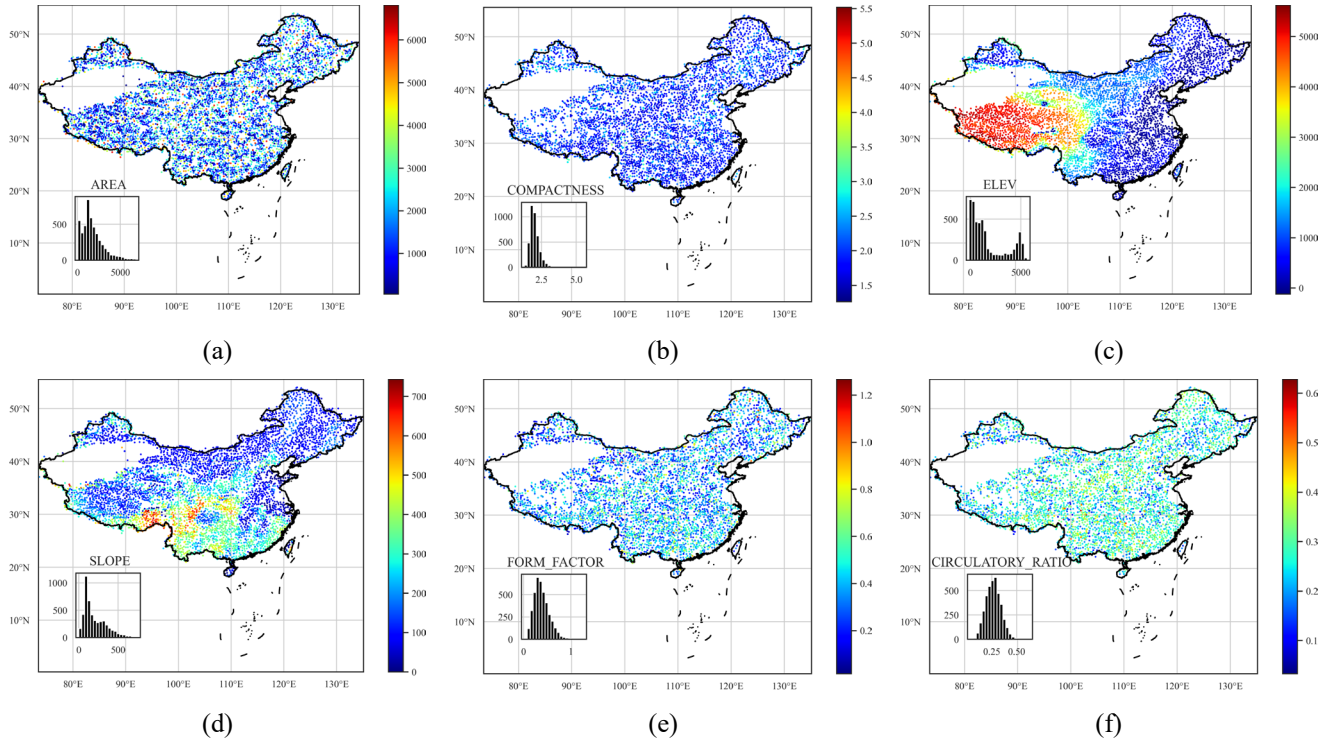

Figure 6. Distributions of topographic characteristics.

The CAMELS dataset provides two parameters (i.e., two area estimates) to describe the catchment shape. The physical characteristics of a catchment can affect the streamflow volume and the streamflow hydrograph of the catchment under a storm. To provide a complete description of the catchment shape, we computed several geometrical parameters of the catchment related to the streamflow process (Fig. 6), including the catchment form factor, shape factor, compactness coefficient, circulatory ratio and elongation ratio (Subramanya, 2013). A summary of the location and topography attributes can be found in Table A1.

7 Soil

The proposed dataset has a total of 54 soil attributes (Table A1) derived from (Hengl et al., 2017; Dai et al., 2019; Shangguan et al., 2013). Five categories of soil characteristics (pH in H2O, organic carbon content, depth to bedrock, cation-exchange capacity, and bulk density) are determined from SoilGrids. SoilGrids (Hengl, Mendes de Jesus et al. 2017) provides global predictions for soil properties, including organic carbon, bulk density, cation exchange capacity (CEC), pH, soil texture

fractions and coarse fragments, by fusing multiple data sources, including MODIS land products, SRTM DEM, climatic images and global landform and lithology maps, at 250 m resolution (Fig. 7). SoilGrids makes predictions using machine learning algorithms and many covariate layers primarily derived from remote sensing data and has soil characteristics at several soil depths.

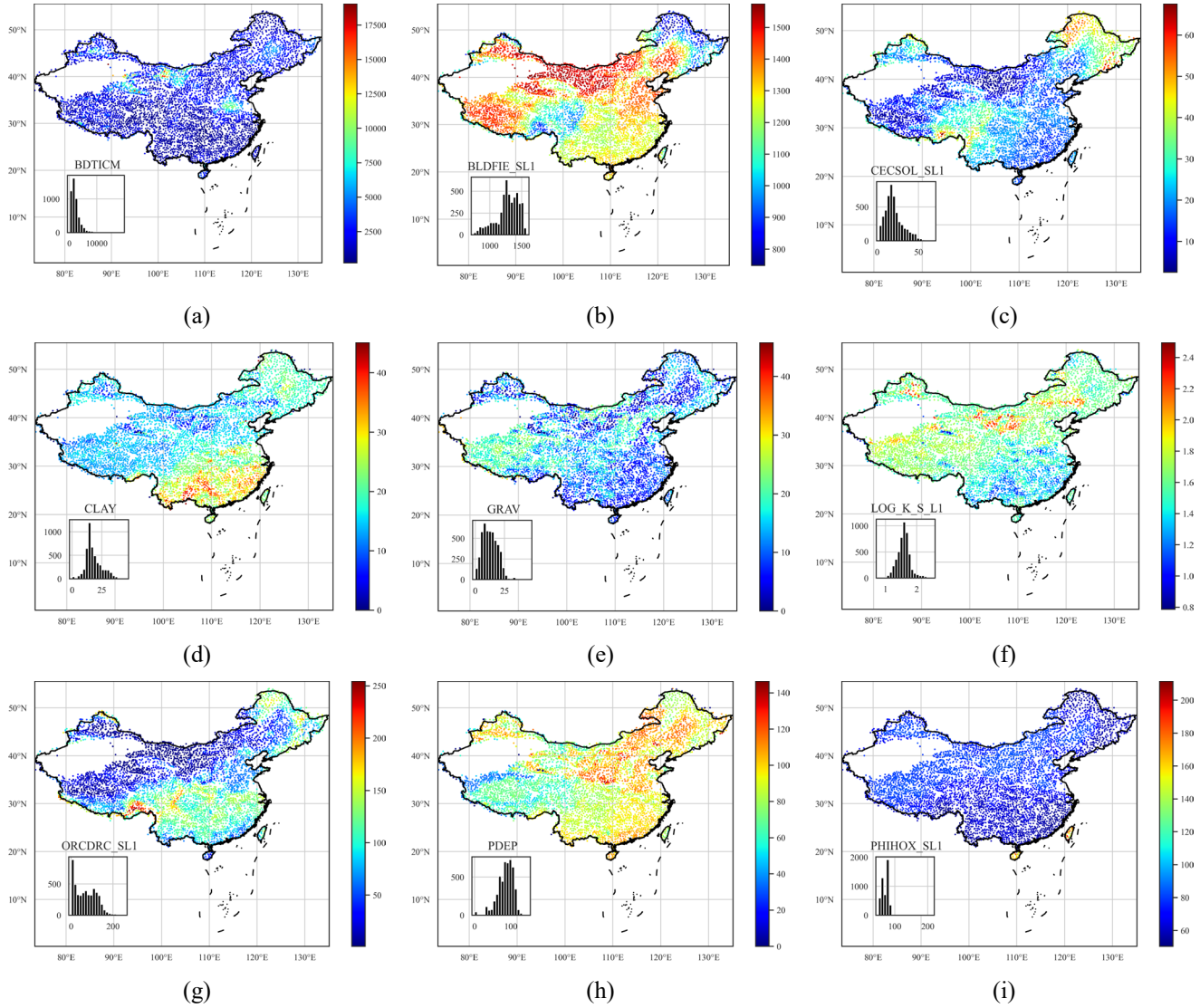

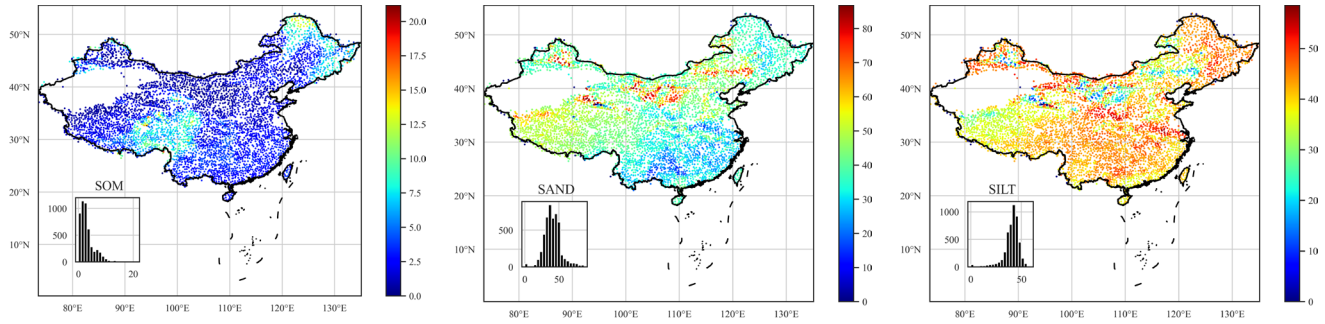

(j) (k) (l)

Figure 7: Distributions of soil characteristics over China.

Unlike CAMELS, whose reported results are obtained by a linear weighted combination of the different soil layers, and CAMELS-BR, whose products are soil characteristics at a depth of 30 cm, we computed soil characteristics at all soil layers provided by SoilGrids250 m.

We determined the saturated water content and saturated hydraulic conductivity (Dai et al., 2019). Based on the same dataset, we also introduced the thermal conductivity of unfrozen saturated soils. Dai et al. (2019) provide a global estimation of soil hydraulic and thermal parameters using multiple Pedotransfer Functions (PTFs) based on the SoilGrids250 m dataset. Based on the SoilGrids250 m and GSDE (Shangguan et al., 2014) datasets, Dai et al. (2019) produce six soil layers with a spatial resolution of 30×30 arc-seconds. Their vertical resolution is the same as that of SoilGrids250 m, with six intervals of 0–0.05 m, 0.05–0.15 m, 0.15–0.30 m, 0.30–0.60 m, 0.60–1.00 m, and 1.00–2.00 m. We determined and recorded catchment soil characteristics for all these layers. In addition, we determined seven more soil characteristics (Shangguan et al., 2013), including soil profile depth, porosity, clay/silt/sand content, rock fragment, and soil organic carbon content. Shangguan et al. (2013) provide the physical and chemical attributes of soils derived from 8,979 soil profiles at a 30×30 arc-second resolution using the polygon linkage method to derive the spatial distribution of soil properties. The profile attribute database and soil map are linked under a framework to avoid uncertainty in taxon referencing.

Depth to bedrock controls many physical and chemical processes in soil. The distribution of depth to bedrock in China is characterized by (i) low values in mountainous areas, such as Yunnan Province and Chongqing City, and (ii) high values in barren areas, such as North and Northwest China. The introduced soil pH value is crucial since it influences many other physical and chemical soil characteristics. The spatial variability of soil pH in China is characterized by (i) soils in southern China being acidic to strongly acidic, (ii) soils in northern China being natural or alkaline, and (iii) soils in northeastern forested areas also being acidic (pH < 7.2). Cation exchange capacity can be seen as a measure of soil fertility since it measures how much nutrient content the soil can store such that it influences the growth of vegetation. Cation exchange capacity is positively correlated with soil organic matter and clay content and is generally low in sandy and silty soils. The spatial variability of

cation exchange capacity in China is characterized by (i) high values in peat and forested areas in the Qinghai-Tibet Plateau, central and northeast China and (ii) extremely low cation exchange capacity in desert areas such as the northwest. Soil hydraulic and thermal properties are greatly affected by soil organic matter (SOM). Soil organic matter has a similar distribution to cation exchange capacity in that it is high in the peat and forested areas in northeast China and low in the north and northwest.

8 Meteorological time series

Table 3: Summary table of catchment meteorological time series available in the proposed dataset

Variable	Description	Unit
prs	catchment daily averaged ground pressure	hPa
tem	catchment daily averaged temperature at 2 m above ground	°C
rhu	catchment daily averaged relative humidity	-
pre	catchment daily averaged precipitation	mm d^{-1}
evp	catchment daily averaged evaporation measured by ground instruments	mm d^{-1}
win	catchment daily averaged wind speed at 2 m above ground	m s^{-1}
ssd	catchment daily averaged sunshine duration	h d^{-1}
gst	catchment daily averaged ground surface temperature	°C
pet	catchment daily averaged potential evapotranspiration determined by Penman's equation (Appendix A)	mm d^{-1}

There have been many studies based on SURF_CLI_CHN_MUL_DAY in China (Xu et al., 2009; Liu et al., 2004; Huang et al., 2016; Liu et al., 2017), such as a trend analysis of pan evaporation (Liu et al., 2010). Nevertheless, there has not yet been a large-scale basin-oriented meteorological time series dataset in China. Researchers need to complete multiple iterations to extract historical meteorological data from the SURF_CLI_CHN_MUL_DAY dataset for this type of research. For the first time, we release a catchment-scale meteorological time series dataset. The open source code can generate any catchment's meteorological time series within China. The basin-oriented dataset provides meteorological time series for 4,911 basins from 1990 to 2020 based on the China Meteorological Data source. Meteorological time series include pressure, temperature, relative humidity, precipitation, evaporation, wind speed, sunshine duration, ground surface temperature and potential evapotranspiration (Table 3).

The meteorological time series data from 1951 to 2010 are derived based on the "1951-2010 China National Ground Station Data Corrected Monthly Data File Basic Data Collection" data construction project. Other data include monthly reported data

to the National Meteorological Information Centre by province and hourly and daily data uploaded by automatic ground stations in real time. During the construction of the dataset, missing data were filled by interpolating to the nearest stations.

Figure 2 presents the variation in the number of sites. The earliest recording was in 1951, but because the early site distribution was sparse, we only used records from 1990 to 2020 to ensure data quality. Inverse distance weighting shows better performance than other interpolation methods. In addition, potential evapotranspiration (PET) is estimated based on Penman's equation (Appendix A) and other meteorological variables.

9 HydroMLYR: Hydrology dataset for Machine Learning in YRB

In addition to the basinwise static attributes provided in CCAM, we propose HydroMLYR, a hydrology dataset for machine learning research in the YRB (Fig. 1). HydroMLYR includes standardized streamflow measurements for 102 basins. The streamflow data are seven-day averaged and standardized basinwise to have zero mean and a standard deviation of 1 (Fig. 8). The HydroMLYR dataset is proposed to support machine learning or deep learning hydrology research (e.g., neural network-based and tree-based algorithms) and can be used in two cases: (i) to develop machine learning models on the YRB or (ii) when it is desirable to verify the generalization ability of a machine learning model on the YRB.

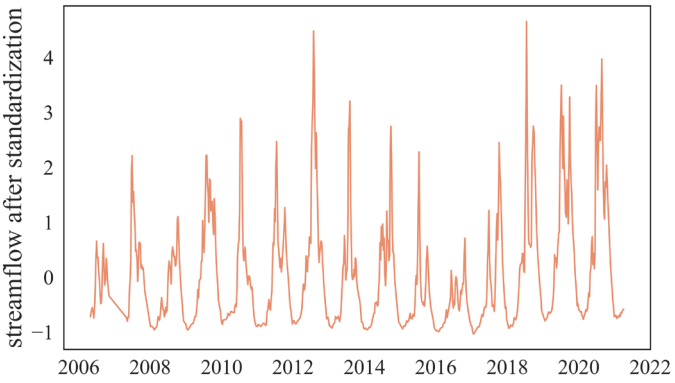

Figure 8: Example of standardized runoff

The dataset provides 40 natural basins that are not affected by reservoirs and dams. The selection is based on a newer version[2] of the Global Reservoirs and Dams database (Lehner et al., 2011), which provides the locations of reservoirs and dams globally. HydroMLYR covers 102 basins in the YRB, including basin boundary shapefiles, static attributes, and standardized streamflow measurements for each basin. The covered basins have areas ranging from 134 to 804,421 square kilometers. Therefore,

[2] http://globaldamwatch.org/data/#core_global

modeling the YRB on a large scale is also possible. Meteorological records in HydroMLYR introduced daily maxima and minima for some forcing variables (Table 4).

The original streamflow observations are not continuous. The average record length is 11.3 years. Although the development of machine learning models does not necessarily require the data to be continuous, we separately provide continuous streamflow observations with an average record length of 8.3 years.

Table 4: Meteorological variables provided in HydroMLYR

Attribute name	Description	Unit
evp	catchment daily averaged evaporation (observations)	mm d^{-1}
gst_mean	catchment daily averaged ground surface temperature	°C
gst_min	catchment daily minimum ground surface temperature	°C
gst_max	catchment daily maximum ground surface temperature	°C
pre	catchment daily averaged precipitation	mm d^{-1}
prs_mean	catchment daily averaged ground surface pressure	hPa
prs_max	catchment daily maximum ground surface pressure	hPa
prs_min	catchment daily minimum ground surface pressure	hPa
rhu	catchment daily averaged relative humidity	-
ssd	catchment daily averaged sunshine duration	h
tem_mean	catchment daily averaged temperature	°C
tem_min	catchment daily minimum temperature	°C
tem_max	catchment daily maximum temperature	°C
win_max	catchment daily maximum wind speed	m s^{-1}
win_mean	catchment daily averaged wind speed	m s^{-1}

10 Data and code availability

The proposed dataset is freely available at http://doi.org/10.5281/zenodo.5137288. The files provided are: (i) several separate files containing 120+ catchment attributes, (ii) the daily meteorological time series in a zip file, (iii) the catchment boundaries used to compute the attributes and extract the time series, (iv) the HydroMLYR dataset, (v) an attribute description file, and (v) a readme file.

11 Conclusion

The CCAM dataset proposed in this paper provides a novel dataset for hydrological research in China. All basins delaminated from the DEM are studied, covering the whole of China. The dataset includes daily meteorological forcing time-series data, including precipitation, temperature, potential evapotranspiration, wind, ground surface temperature, pressure, humidity, sunshine duration and the derived potential evapotranspiration of 4,911 catchments. The proposed time series dataset is derived from the quality-controlled SURF_CLI_CHN_MUL_DAY dataset. CCAM includes 120+ catchment attributes, including soil, land cover, geology, climate indices and topography for each catchment. We produced a series of maps depicting the catchment attribute distributions in China. These maps present regional changes in various features; we also estimated the relationships between them based on Kendall's correlation. Integrating multiple data sources into one dataset at a catchment scale simplifies the data compilation process in research. CCAM can help test hypotheses and formulate valid conclusions under various conditions (i.e., not limited to a few specific locations only) and help explore how different basin characteristics influence hydrological behaviors, learn the migration of hydrological behaviors between different basins, and develop general frameworks for large-scale model evaluation and benchmarking in China. A limitation of this study is its failure to estimate the uncertainty of the meteorological time series. An alternative is to evaluate the uncertainty of the basinwise meteorological data based on multiple independent data sources, but there are few data sources that provide as many data types as SURF_CLI_CHN_MUL_DAY. Hence, evaluating the uncertainty of these eight meteorological variables poses a challenge that is left for future studies.

Appendix A: Attributes summary

Table A1: Summary table of catchment attributes available in the proposed dataset.

Attribute class	Attribute name	Description	Unit	Data source
Climate indices (computed for 1 Oct 1990 to 30 Sep 2018)	pet_mean	mean daily pet (Penman–Monteith equation)	mm d^{-1}	Subramanya (2013)
	evp_mean	mean daily evaporation (observations)	mm d^{-1}	SURF_CLI_CHN_MUL_DAY
	gst_mean	mean daily ground surface temperature	°C	
	pre_mean	mean daily precipitation	mm d^{-1}	
	prs_mean	mean daily ground surface pressure	hPa	
	rhu_mean	mean daily relative humidity	-	
	ssd_mean	mean daily sunshine duration	h	

tem_mean	mean daily temperature	°C
win_mean	mean daily wind speed	m s^{-1}
p_seasonality	seasonality and timing of precipitation (estimated using sine curves to represent the annual temperature and precipitation cycles, positive [negative] values indicate that precipitation peaks in summer [winter], values close to 0 indicate uniform precipitation throughout the year)	-
high_prec_freq	frequency of high-precipitation days (⩾ 5 times mean daily precipitation)	d yr^{-1}
high_prec_dur	average duration of high-precipitation events (number of consecutive days ⩾ 5 times mean daily precipitation)	d
high_prec_timing	season during which most high-precipitation days (⩾ 5 times mean daily precipitation) occur	season
low_prec_freq	frequency of dry days (< 1mm d^{-1})	d yr^{-1}
low_prec_dur	average duration of dry periods (number of consecutive days < 1 mm d^{-1})	d
low_prec_timing	season during which most dry days (< 1 mm d^{-1}) occur	season
frac_snow_daily	fraction of precipitation falling as snow (for days colder than 0 °C)	-
p_seasonality	seasonality and timing of precipitation, positive [negative] values indicate that precipitation peaks in summer [winter], values	-

		close to 0 indicate uniform precipitation throughout the year		
Geological characteristics	geol_porosity	subsurface porosity	-	Gleeson et al. (2014)
	geol_permeability	subsurface permeability (log-10)	m^2	
	ig	fraction of the catchment area associated with ice and glaciers	-	Hartmann and Moosdorf (2012)
	pa	fraction of the catchment area associated with acid plutonic rocks	-	
	sc	fraction of the catchment area associated with carbonate sedimentary rocks	-	
	su	fraction of the catchment area associated with unconsolidated sediments	-	
	sm	fraction of the catchment area associated with mixed sedimentary rocks	-	
	vi	fraction of the catchment area associated with intermediate volcanic rocks	-	
	mt	fraction of the catchment area associated with metamorphic	-	
	ss	fraction of the catchment area associated with siliciclastic sedimentary rocks	-	
	pi	fraction of the catchment area associated with intermediate plutonic rocks	-	
	va	fraction of the catchment area associated with acid volcanic rocks	-	
	wb	fraction of the catchment area associated with water bodies	-	

	pb	fraction of the catchment area associated with basic plutonic rocks	-	
	vb	fraction of the catchment area associated with basic volcanic rocks	-	
	nd	fraction of the catchment area associated with no data	-	
	py	fraction of the catchment area associated with pyroclastic	-	
	ev	fraction of the catchment area associated with evaporites	-	
Land cover characteristics	lai_max	maximum monthly mean of the leaf area index (based on 12 monthly means)	-	Myneni et al. (2015)
	lai_diff	difference between the maximum and minimum monthly mean of the leaf area index (based on 12 monthly means)	-	
	ndvi_mean	mean normalized difference vegetation index (NDVI)	-	Didan (2015)
	root_depth_50	root depth (percentiles=50% extracted from a root depth distribution based on IGBP land cover)	m	Eq. 2 and Table 2 in (Zeng, 2001)
	root_depth_99	root depth (percentiles=99% extracted from a root depth distribution based on IGBP land cover)	m	
	evergreen needleleaf tree	catchment area fraction covered by evergreen needleleaf tree	-	Sulla-Menashe and Friedl (2018)
	evergreen broadleaf tree	catchment area fraction covered by evergreen broadleaf tree	-	

	deciduous needleleaf tree	catchment area fraction covered by deciduous needleleaf forests	-	
	deciduous broadleaf tree	catchment area fraction covered by deciduous broadleaf tree	-	
	mixed forest	catchment area fraction covered by mixed forest	-	
	closed shrubland	catchment area fraction covered by closed shrubland	-	
	open shrubland	catchment area fraction covered by open shrubland	-	
	woody savanna	catchment area fraction covered by woody savanna	-	
	savanna	catchment area fraction covered by savanna	-	
	grassland	catchment area fraction covered by grassland	-	
	permanent wetland	catchment area fraction covered by permanent wetland	-	
	cropland	catchment area fraction covered by cropland	-	
	urban and built-up land	catchment area fraction covered by urban and built-up land	-	
	cropland/natural vegetation	catchment area fraction covered by cropland/natural vegetation	-	
	snow and ice	catchment area fraction covered by snow and ice	-	
	barren	catchment area fraction covered by barren	-	
	water bodies	catchment area fraction covered by water bodies	-	
Topography, location and	basin_id	drainage basin identifiers	-	Masutomi et al. (2009)
	pop	population	people	
	pop_dnsty	population density	people km^{-2}	

Human intervention	lat	mean latitude	°N	
	lon	mean longitude	°E	
	elev	mean elevation	M	
	area	catchment area	km^2	
	slope	mean slope	$m\ km^{-1}$	Horn (1981)
	length	The length of the mainstream measured from the basin outlet to the remotest point on the basin boundary. The mainstream is identified by starting from the basin outlet and moving up the catchment.	km	Subramanya (2013)
	form factor	catchment area / (catchment length)^2	-	
	shape factor	(catchment length)^2 / catchment area	-	
	compactness coefficient	perimeter of the catchment / perimeter of the circle whose area is that of the basin	-	
	circulatory ratio	catchment area / area of circle of catchment perimeter	-	
	elongation ratio	diameter of circle whose area is basin area / catchment length	-	
Soil	pdep	soil profile depth	cm	Shangguan et al. (2013)
	clay	percentage of clay content of the soil material	%	
	sand	percentage of sand content of the soil material	%	
	por	porosity	$cm^3\ cm^{-3}$	
	silt	percentage of silt content of the soil material	%	
	grav	rock fragment content	%	
	som	soil organic carbon content	%	

	log_k_s4F[3]	log-10 transformation of saturated hydraulic conductivity	cm d^{-1}	Dai et al. (2019)
	theta_s[4]	saturated water content	cm^3 cm^{-3}	
	tksatu[4]	thermal conductivity of unfrozen saturated soils	W m^{-1} K^{-1}	
	bldfie[4]	bulk density	kg m^{-3}	Hengl et al. (2017)
	cecsol[4]	cation-exchange capacity	cmol+ kg^{-1}	
	orcdrc[4]	organic carbon content	g kg^{-1}	
	phihox[4]	pH in H2O	10^{-1}	
	bdticm	depth to bedrock	cm	

Appendix B: Modified Penman's equation

Penman's equation (Subramanya, 2013), incorporating some modifications to the original formula, is:

$$PET = \frac{AH_n + E_a\gamma}{A + \gamma}$$

where PET is the daily potential evapotranspiration in mm per day; A is the slope of the saturation vapor pressure (ew) vs. temperature (t) curve at the mean air temperature, in mm of mercury per Celsius; Hn is the net radiation in mm of evaporable water per day; Ea is a parameter including wind speed and saturation deficit; and γ is the psychrometric constant = 0.49 mm of mercury per Celsius.

The relationship between ew and t is defined as:

$$e_w = 4.584 \exp\left(\frac{17.27t}{237.3 + t}\right)$$

The following equation estimates the net radiation:

$$H_n = H_a(1 - r)\left(a + b\frac{n}{N}\right) - \sigma T_a^4\left(0.56 - 0.092\sqrt{e_a}\right)\left(0.10 + 0.90\frac{n}{N}\right)$$

where Ha is the incident solar radiation outside the atmosphere on a horizontal surface, expressed in mm of evaporable water per day (a function of the latitude and period of the year as indicated in Table B1); a is a constant depending upon the latitude ϕ and is given by $a = 0.29\ cos\ \phi$; b is a constant = 0.52; n is the sunshine duration in hours; N is the maximum possible hours of bright sunshine (a function of latitude, see Table B2); r is the reflection coefficient; σ is the Stefan-Boltzman constant

[3] The data source contains multi-layer soil data, soil characteristics for all layers are determined.

= 2.01×10^{-9} mm/day; Ta is the mean air temperature in degrees kelvin; ea is the actual mean vapor pressure in the air in mm of mercury.

Table B1: Mean Monthly Solar Radiation, Ha in mm of Evaporable Water/Day

North latitude	Jan	Feb	Mar	Apr	May	Jun	Jul	Aug	Sep	Oct	Nov	Dec
0°	14.5	15.0	15.2	14.7	13.9	13.4	13.5	14.2	14.9	15.0	14.6	14.3
10°	12.8	13.9	14.8	15.2	15.0	14.8	14.8	15.0	14.9	14.1	13.1	12.4
20°	10.8	12.3	13.9	15.2	15.7	15.8	15.7	15.3	14.4	12.9	11.2	10.3
30°	8.5	10.5	12.7	14.8	16.0	16.5	16.2	15.3	13.5	11.3	9.1	7.9
40°	6.0	8.3	11.0	13.9	15.9	16.7	16.3	14.8	12.2	9.3	6.7	5.4
50°	3.6	5.9	9.1	12.7	15.4	16.7	16.1	13.9	10.5	7.1	4.3	3.0

The parameter Ea is estimated as:

$$E_a = 0.35\left(1 + \frac{u_2}{160}\right)(e_w - e_a)$$

where $u2$ is the wind speed at $2m$ above ground in km/day; ew is the saturation vapor pressure at mean air temperature in mm of mercury; and ea is the actual vapor pressure.

Table B2: Mean Monthly Values of Possible Sunshine Hours, N

North latitude	Jan	Feb	Mar	Apr	May	Jun	Jul	Aug	Sep	Oct	Nov	Dec
0°	12.1	12.1	12.1	12.1	12.1	12.1	12.1	12.1	12.1	12.1	12.1	12.1
10°	11.6	11.8	12.1	12.4	12.6	12.7	12.6	12.4	12.9	11.9	11.7	11.5
20°	11.1	11.5	12.0	12.6	13.1	13.3	13.2	12.8	12.3	11.7	11.2	10.9
30°	10.4	11.1	12.0	12.9	13.7	14.1	13.9	13.2	12.4	11.5	10.6	10.2
40°	9.6	10.7	11.9	13.2	14.4	15.0	14.7	13.8	12.5	11.2	10.0	9.4
50°	8.6	10.1	11.8	13.8	15.4	16.4	16.0	14.5	12.7	10.8	9.1	8.1

Appendix C: Correlation analysis of catchment attributes

To explore the potential connections between various types of watershed attributes, we performed correlation analysis using the Kendall rank correlation coefficient (Kendall, 1938). The Kendall rank correlation coefficient is a measure of rank correlation: the similarity of the sort order of the two sets of data. Kendall correlation will be high if the orderings of the observations of two variables are similar. Kendall correlation avoids the assumption of a linear relationship and that the distribution should be normal and continuous (e.g., Pearson correlation). When the relationship is not exactly linear, using

Pearson correlation will miss out on information that Kendall could capture. Table C1 shows the top five most relevant attributes for each attribute. The analysis result shows that the correlations between variables are in line with general understanding, justifying the rationality of the dataset, to name a few:

(1) Subsurface permeability and porosity are most correlated with geological attributes.

(2) LAI and NDVI are most positively correlated with each other but most negatively correlated with the fraction of barren land cover.

(3) Urban and built ups are most positively correlated with population density.

(4) In China, the savanna is mainly distributed in the southern coastal areas, resulting in it being most positively correlated with mean precipitation.

(5) Sand is most positively correlated with saturated hydraulic conductivity, while clay is strongly negatively correlated with saturated hydraulic conductivity.

Table C1: The top five most relevant characteristics for each attribute (different soil layers for the same attribute are excluded, e.g., phihox_sl2 is not included in the top five most relevant attributes of phihox_sl1, although they are highly correlated)

Attribute	1st	2nd	3rd	4th	5th
high_prec_freq	root_depth_50(-0.196)	grassland(0.175)	root_depth_99(-0.171)	som(0.136)	tksatu_l1(-0.133)
high_prec_dur	theta_s_l6(-0.277)	theta_s_l5(-0.234)	p_seasonality(0.233)	elev(0.211)	theta_s_l4(-0.201)
low_prec_freq	pre_mean(-0.766)	aridity(0.745)	ssd_mean(0.652)	rhu_mean(-0.627)	phihox_sl7(0.588)
low_prec_dur	aridity(0.78)	pre_mean(-0.768)	ssd_mean(0.731)	rhu_mean(-0.709)	phihox_sl7(0.579)
frac_snow_daily	gst_mean(-0.802)	tem_mean(-0.792)	lat(0.575)	evergreen_broadleaf_tree(-0.512)	pre_mean(-0.436)
prs_mean	elev(-0.678)	lon(0.552)	rhu_mean(0.432)	urban_and_built-up_land(0.427)	barren(-0.41)
pre_mean	aridity(-0.913)	low_prec_dur(-0.768)	low_prec_freq(-0.766)	ssd_mean(-0.723)	rhu_mean(0.712)
evp_mean	aridity(0.643)	ndvi_mean(-0.632)	rhu_mean(-0.617)	ssd_mean(0.598)	lai_dif(-0.593)
gst_mean	tem_mean(0.924)	frac_snow_daily(-0.802)	lat(-0.512)	evergreen_broadleaf_tree(0.507)	pet_mean(0.442)
rhu_mean	aridity(-0.751)	ssd_mean(-0.746)	pre_mean(0.712)	low_prec_dur(-0.709)	low_prec_freq(-0.627)
pet_mean	cecsol_sl2(-0.451)	gst_mean(0.442)	cecsol_sl3(-0.441)	cecsol_sl1(-0.422)	cecsol_sl4(-0.42)

ssd_mean	aridity(0.753)	rhu_mean(-0.746)	low_prec_dur(0.731)	pre_mean(-0.723)	low_prec_freq(0.652)
win_mean	ssd_mean(0.426)	woody_savanna(-0.393)	tem_mean(-0.379)	gst_mean(-0.377)	mixed_forest(-0.363)
tem_mean	gst_mean(0.924)	frac_snow_daily(-0.792)	evergreen_broadleaf_tree(0.493)	pop_dnsty(0.475)	lat(-0.474)
p_seasonality	rhu_mean(-0.421)	tem_mean(-0.397)	gst_mean(-0.393)	ssd_mean(0.393)	low_prec_dur(0.375)
aridity	pre_mean(-0.913)	low_prec_dur(0.78)	ssd_mean(0.753)	rhu_mean(-0.751)	low_prec_freq(0.745)
slope	lat(-0.374)	bdticm(-0.348)	win_mean(-0.341)	mixed_forest(0.341)	evergreen_needleleaf_tree(0.327)
lon	elev(-0.585)	prs_mean(0.552)	evp_mean(-0.5)	barren(-0.482)	ndvi_mean(0.47)
elev	prs_mean(-0.678)	lon(-0.585)	urban_and_built-up_land(-0.485)	pop_dnsty(-0.481)	cropland(-0.456)
lat	frac_snow_daily(0.575)	evergreen_broadleaf_tree(-0.548)	gst_mean(-0.512)	tem_mean(-0.474)	low_prec_freq(0.437)
pop	urban_and_built-up_land(0.618)	cropland(0.519)	aridity(-0.511)	pre_mean(0.505)	rhu_mean(0.492)
pop_dnsty	urban_and_built-up_land(0.639)	aridity(-0.538)	cropland(0.533)	pre_mean(0.533)	ssd_mean(-0.521)
length	area(0.684)	form_factor(-0.398)	shape_factor(0.398)	elongation_ratio(-0.398)	compactness_coefficient(0.363)
area	length(0.684)	pop(0.23)	pa(0.194)	circulatory_ratio(-0.187)	compactness_coefficient(0.187)
form_factor	elongation_ratio(1.0)	shape_factor(-1.0)	circulatory_ratio(0.435)	compactness_coefficient(-0.435)	length(-0.398)
shape_factor	elongation_ratio(-1.0)	form_factor(-1.0)	circulatory_ratio(-0.435)	compactness_coefficient(0.435)	length(0.398)
compactness_coefficient	circulatory_ratio(-1.0)	elongation_ratio(-0.435)	shape_factor(0.435)	form_factor(-0.435)	length(0.363)
circulatory_ratio	compactness_coefficient(-1.0)	elongation_ratio(0.435)	shape_factor(-0.435)	form_factor(0.435)	length(-0.363)

elongation_ratio	shape_factor(-1.0)	form_factor(1.0)	circulatory_ratio(0.435)	compactness_coefficient(-0.435)	length(-0.398)
lai_dif	ndvi_mean(0.808)	barren(-0.642)	aridity(-0.638)	pre_mean(0.609)	woody_savanna(0.607)
lai_max	ndvi_mean(0.779)	barren(-0.614)	aridity(-0.613)	woody_savanna(0.612)	phihox_sl2(-0.602)
ndvi_mean	lai_dif(0.808)	lai_max(0.779)	barren(-0.677)	evp_mean(-0.632)	aridity(-0.607)
root_depth_50	grassland(-0.485)	pet_mean(0.232)	barren(0.212)	high_prec_freq(-0.196)	pdep(-0.176)
root_depth_99	grassland(-0.339)	barren(0.337)	cropland(-0.336)	pdep(-0.284)	lon(-0.283)
evergreen_needleleaf_tree	mixed_forest(0.572)	woody_savanna(0.481)	phihox_sl7(-0.416)	phihox_sl6(-0.411)	phihox_sl5(-0.409)
evergreen_broadleaf_tree	lat(-0.548)	phihox_sl7(-0.538)	phihox_sl6(-0.529)	phihox_sl5(-0.522)	pre_mean(0.512)
deciduous_needleleaf_tree	cecsol_sl1(0.274)	bldfie_sl1(-0.274)	cecsol_sl2(0.272)	orcdrc_sl2(0.27)	cecsol_sl3(0.262)
deciduous_broadleaf_tree	mixed_forest(0.604)	woody_savanna(0.568)	ndvi_mean(0.524)	lai_max(0.5)	lai_dif(0.497)
mixed_forest	woody_savanna(0.713)	deciduous_broadleaf_tree(0.604)	evergreen_needleleaf_tree(0.572)	phihox_sl7(-0.565)	phihox_sl6(-0.563)
closed_shrubland	deciduous_broadleaf_tree(0.217)	savanna(0.16)	mixed_forest(0.158)	tksatu_l4(-0.153)	theta_s_l2(-0.142)
open_shrubland	high_prec_dur(0.179)	rhu_mean(-0.174)	elev(0.17)	ssd_mean(0.17)	prs_mean(-0.165)
woody_savanna	mixed_forest(0.713)	phihox_sl7(-0.628)	phihox_sl4(-0.628)	phihox_sl3(-0.627)	phihox_sl6(-0.627)
savanna	pre_mean(0.606)	cropland_natural_vegetaion(0.605)	woody_savanna(0.604)	aridity(-0.602)	ssd_mean(-0.591)
grassland	root_depth_50(-0.485)	cropland_natural_vegetaion(-0.363)	tem_mean(-0.344)	gst_mean(-0.344)	root_depth_99(-0.339)
permanent_wetland	water_bodies(0.469)	savanna(0.363)	urban_and_built-up_land(0.347)	pre_mean(0.343)	pop(0.343)

cropland	urban_and_built-up_land(0.546)	pop_dnsty(0.533)	pop(0.519)	elev(-0.456)	lon(0.417)
urban_and_built-up_land	pop_dnsty(0.639)	pop(0.618)	cropland(0.546)	elev(-0.485)	cropland_natural_vegetaion(0.428)
cropland_natural_vegetaion	savanna(0.605)	rhu_mean(0.546)	aridity(-0.523)	ssd_mean(-0.52)	pre_mean(0.51)
snow_and_ice	ig(0.431)	barren(0.379)	lon(-0.373)	elev(0.369)	pdep(-0.354)
barren	ndvi_mean(-0.677)	lai_dif(-0.642)	lai_max(-0.614)	aridity(0.581)	evp_mean(0.574)
water_bodies	permanent_wetland(0.469)	wb(0.39)	cropland_natural_vegetaion(0.17)	urban_and_built-up_land(0.158)	elev(-0.154)
geol_permeability	sm(-0.345)	su(0.326)	ss(-0.316)	bdticm(0.228)	pdep(0.161)
geol_porosity	su(0.455)	pa(-0.417)	woody_savanna(-0.323)	phihox_sl3(0.315)	phihox_sl4(0.314)
ig	snow_and_ice(0.431)	elev(0.194)	theta_s_l2(-0.185)	pdep(-0.184)	theta_s_l3(-0.182)
pa	geol_porosity(-0.417)	mt(0.3)	pi(0.295)	va(0.271)	vi(0.246)
sc	geol_porosity(-0.285)	lat(-0.264)	bdticm(-0.26)	slope(0.246)	mixed_forest(0.231)
su	bdticm(0.52)	geol_porosity(0.455)	woody_savanna(-0.349)	geol_permeability(0.326)	phihox_sl7(0.326)
sm	geol_permeability(-0.345)	su(-0.283)	bdticm(-0.228)	cropland(-0.199)	elev(0.194)
vi	pa(0.246)	pi(0.203)	va(0.171)	geol_porosity(-0.169)	deciduous_broadleaf_tree(0.166)
mt	pa(0.3)	geol_porosity(-0.286)	pi(0.199)	deciduous_broadleaf_tree(0.187)	area(0.18)
ss	geol_permeability(-0.316)	su(-0.17)	bdticm(-0.136)	evergreen_needleleaf_tree(0.106)	tksatu_l6(-0.096)
pi	pa(0.295)	vi(0.203)	mt(0.199)	geol_porosity(-0.183)	va(0.172)

va	pa(0.271)	geol_porosity(-0.219)	vb(0.21)	deciduous_needle leaf_tree(0.186)	pi(0.172)
wb	water_bodies(0.39)	permanent_wetland(0.264)	bldfie_sl4(0.148)	bldfie_sl5(0.147)	urban_and_built-up_land(0.138)
pb	mt(0.176)	pa(0.132)	theta_s_l5(-0.128)	area(0.127)	length(0.123)
vb	va(0.21)	geol_porosity(-0.171)	vi(0.165)	cecsol_sl7(0.161)	cecsol_sl6(0.157)
nd	barren(0.154)	aridity(0.146)	pre_mean(-0.144)	lai_dif(-0.141)	snow_and_ice(0.141)
py	phihox_sl1(-0.237)	phihox_sl2(-0.233)	phihox_sl3(-0.233)	phihox_sl4(-0.23)	woody_savanna(0.227)
ev	barren(0.036)	orcdrc_sl5(-0.035)	orcdrc_sl4(-0.035)	cecsol_sl3(-0.034)	orcdrc_sl7(-0.034)
tksatu_l1	grav(-0.346)	som(-0.344)	bldfie_sl3(0.298)	bldfie_sl1(0.295)	bldfie_sl2(0.291)
tksatu_l2	som(-0.365)	bldfie_sl3(0.326)	bldfie_sl1(0.326)	bldfie_sl2(0.323)	grav(-0.308)
tksatu_l3	som(-0.344)	bldfie_sl2(0.328)	bldfie_sl1(0.325)	bldfie_sl3(0.324)	bldfie_sl4(0.308)
tksatu_l4	bldfie_sl2(0.398)	som(-0.397)	bldfie_sl1(0.388)	bldfie_sl3(0.384)	bldfie_sl4(0.358)
tksatu_l5	bldfie_sl3(0.386)	bldfie_sl2(0.376)	som(-0.369)	bldfie_sl4(0.364)	bldfie_sl1(0.358)
tksatu_l6	bldfie_sl3(0.366)	som(-0.362)	bdticm(0.36)	bldfie_sl2(0.343)	bldfie_sl7(0.338)
log_k_s_l1	sand(0.71)	clay(-0.59)	savanna(-0.441)	silt(-0.436)	rhu_mean(-0.423)
log_k_s_l2	sand(0.709)	clay(-0.578)	savanna(-0.452)	phihox_sl7(0.438)	silt(-0.433)
log_k_s_l3	sand(0.682)	clay(-0.592)	savanna(-0.448)	phihox_sl7(0.442)	phihox_sl6(0.435)
log_k_s_l4	sand(0.612)	clay(-0.603)	savanna(-0.49)	pre_mean(-0.489)	phihox_sl7(0.485)
log_k_s_l5	clay(-0.561)	sand(0.555)	phihox_sl7(0.506)	savanna(-0.501)	phihox_sl6(0.501)
log_k_s_l6	clay(-0.563)	pre_mean(-0.555)	aridity(0.548)	phihox_sl7(0.534)	phihox_sl6(0.532)
theta_s_l1	grav(-0.582)	clay(0.325)	sand(-0.315)	elev(-0.314)	pdep(0.311)
theta_s_l2	grav(-0.585)	pdep(0.377)	elev(-0.366)	clay(0.35)	sand(-0.326)
theta_s_l3	grav(-0.522)	pdep(0.42)	elev(-0.414)	prs_mean(0.365)	clay(0.359)
theta_s_l4	grav(-0.515)	pdep(0.463)	elev(-0.412)	prs_mean(0.349)	lon(0.328)
theta_s_l5	grav(-0.433)	elev(-0.401)	pdep(0.376)	sand(-0.349)	rhu_mean(0.331)
theta_s_l6	evergreen_broadleaf_tree(0.372)	grav(-0.357)	elev(-0.344)	sand(-0.343)	tem_mean(0.337)

orcdrc_sl7	bldfie_sl4(-0.581)	bldfie_sl5(-0.572)	bldfie_sl6(-0.548)	bldfie_sl3(-0.535)	bldfie_sl7(-0.523)
orcdrc_sl3	bldfie_sl3(-0.738)	bldfie_sl2(-0.728)	bldfie_sl1(-0.701)	bldfie_sl4(-0.691)	bldfie_sl5(-0.621)
orcdrc_sl4	bldfie_sl3(-0.702)	bldfie_sl2(-0.682)	bldfie_sl4(-0.676)	bldfie_sl1(-0.657)	bldfie_sl5(-0.614)
orcdrc_sl5	bldfie_sl4(-0.641)	bldfie_sl3(-0.636)	bldfie_sl2(-0.611)	bldfie_sl5(-0.6)	bldfie_sl1(-0.592)
orcdrc_sl6	bldfie_sl4(-0.584)	bldfie_sl5(-0.567)	bldfie_sl6(-0.556)	bldfie_sl3(-0.552)	bldfie_sl7(-0.534)
orcdrc_sl2	bldfie_sl2(-0.787)	bldfie_sl1(-0.769)	bldfie_sl3(-0.749)	bldfie_sl4(-0.68)	cecsol_sl1(0.629)
orcdrc_sl1	phihox_sl2(-0.599)	phihox_sl3(-0.594)	phihox_sl4(-0.591)	phihox_sl5(-0.586)	phihox_sl6(-0.585)
phihox_sl7	woody_savanna(-0.628)	pre_mean(-0.598)	aridity(0.592)	low_prec_freq(0.588)	orcdrc_sl1(-0.583)
phihox_sl6	woody_savanna(-0.627)	pre_mean(-0.594)	aridity(0.59)	lai_max(-0.587)	orcdrc_sl1(-0.585)
phihox_sl5	woody_savanna(-0.626)	lai_max(-0.593)	pre_mean(-0.592)	aridity(0.589)	orcdrc_sl1(-0.586)
phihox_sl4	woody_savanna(-0.628)	lai_max(-0.599)	orcdrc_sl1(-0.591)	lai_dif(-0.578)	pre_mean(-0.576)
phihox_sl3	woody_savanna(-0.627)	lai_max(-0.595)	orcdrc_sl1(-0.594)	lai_dif(-0.576)	pre_mean(-0.568)
phihox_sl2	woody_savanna(-0.627)	lai_max(-0.602)	orcdrc_sl1(-0.599)	lai_dif(-0.583)	low_prec_freq(0.569)
phihox_sl1	woody_savanna(-0.601)	lai_max(-0.586)	orcdrc_sl1(-0.584)	lai_dif(-0.565)	bldfie_sl2(0.55)
bldfie_sl7	orcdrc_sl5(-0.547)	orcdrc_sl4(-0.546)	orcdrc_sl3(-0.543)	orcdrc_sl6(-0.534)	orcdrc_sl7(-0.523)
bldfie_sl6	orcdrc_sl5(-0.559)	orcdrc_sl6(-0.556)	orcdrc_sl4(-0.553)	orcdrc_sl7(-0.548)	orcdrc_sl3(-0.547)

bldfie_sl5	orcdrc_sl3(-0.621)	orcdrc_sl4(-0.614)	orcdrc_sl5(-0.6)	orcdrc_sl2(-0.597)	orcdrc_sl7(-0.572)
bldfie_sl4	orcdrc_sl3(-0.691)	orcdrc_sl2(-0.68)	orcdrc_sl4(-0.676)	orcdrc_sl5(-0.641)	orcdrc_sl6(-0.584)
bldfie_sl1	orcdrc_sl2(-0.769)	orcdrc_sl3(-0.701)	cecsol_sl1(-0.686)	orcdrc_sl4(-0.657)	som(-0.606)
bldfie_sl3	orcdrc_sl2(-0.749)	orcdrc_sl3(-0.738)	orcdrc_sl4(-0.702)	orcdrc_sl5(-0.636)	som(-0.633)
bldfie_sl2	orcdrc_sl2(-0.787)	orcdrc_sl3(-0.728)	orcdrc_sl4(-0.682)	cecsol_sl1(-0.671)	som(-0.651)
cecsol_sl1	bldfie_sl1(-0.686)	bldfie_sl2(-0.671)	orcdrc_sl2(0.629)	bldfie_sl3(-0.598)	orcdrc_sl3(0.579)
cecsol_sl2	bldfie_sl1(-0.579)	bldfie_sl2(-0.566)	orcdrc_sl2(0.553)	orcdrc_sl3(0.523)	bldfie_sl3(-0.515)
cecsol_sl5	bldfie_sl1(-0.445)	bldfie_sl2(-0.429)	orcdrc_sl2(0.412)	orcdrc_sl3(0.393)	pet_mean(-0.392)
cecsol_sl4	bldfie_sl1(-0.472)	bldfie_sl2(-0.459)	orcdrc_sl2(0.447)	orcdrc_sl3(0.43)	orcdrc_sl5(0.424)
cecsol_sl3	bldfie_sl1(-0.532)	bldfie_sl2(-0.52)	orcdrc_sl2(0.508)	orcdrc_sl3(0.49)	orcdrc_sl4(0.478)
cecsol_sl7	bldfie_sl1(-0.413)	bldfie_sl2(-0.396)	orcdrc_sl2(0.38)	pet_mean(-0.374)	orcdrc_sl3(0.362)
cecsol_sl6	bldfie_sl1(-0.409)	bldfie_sl2(-0.393)	orcdrc_sl2(0.378)	pet_mean(-0.373)	orcdrc_sl3(0.36)
bdticm	su(0.52)	woody_savanna(-0.412)	low_prec_freq(0.382)	phihox_sl7(0.378)	mixed_forest(-0.374)
pdep	theta_s_l4(0.463)	elev(-0.436)	grav(-0.424)	theta_s_l3(0.42)	lon(0.4)
por	som(0.363)	bldfie_sl1(-0.335)	phihox_sl1(-0.329)	phihox_sl3(-0.328)	phihox_sl2(-0.328)
clay	sand(-0.67)	log_k_s_l4(-0.603)	log_k_s_l3(-0.592)	log_k_s_l1(-0.59)	log_k_s_l2(-0.578)
sand	log_k_s_l1(0.71)	log_k_s_l2(0.709)	log_k_s_l3(0.682)	clay(-0.67)	log_k_s_l4(0.612)

silt	sand(-0.573)	log_k_s_l1(-0.436)	log_k_s_l2(-0.433)	log_k_s_l3(-0.4)	log_k_s_l4(-0.316)
grav	theta_s_l2(-0.585)	theta_s_l1(-0.582)	theta_s_l3(-0.522)	theta_s_l4(-0.515)	theta_s_l5(-0.433)
som	bldfie_sl2(-0.651)	bldfie_sl3(-0.633)	bldfie_sl1(-0.606)	orcdrc_sl2(0.599)	orcdrc_sl3(0.576)
high_prec_freq	root_depth_50(-0.196)	grassland(0.175)	root_depth_99(-0.171)	som(0.136)	tksatu_l1(-0.133)
high_prec_dur	theta_s_l6(-0.277)	theta_s_l5(-0.234)	p_seasonality(0.233)	elev(0.211)	theta_s_l4(-0.201)
low_prec_freq	pre_mean(-0.766)	aridity(0.745)	ssd_mean(0.652)	rhu_mean(-0.627)	phihox_sl7(0.588)

Appendix D: Data sources and processing

The program to generate the dataset is mainly written in Python. The rasterio[4] library is used to extract from the raster for the given basin boundary, reproject and merge rasters; The shapely[5] library is used to calculate the geometry; The pyproj[6] library is used for coordinate system conversions; The richdem[7] library is used to calculate slope; The netCDF4[8] and xarray[9] library is used to read the netCDF files; The pyshp[10] library is used to handle shapefiles; The gdal[11] command-line programs are used for data format conversions; The Python multiprocessing[12] library is used for multithreaded data processing such as the calculation of meteorological time series; The interpolation program is written based on SciPy and NumPy. In addition, the calculation of the catchment boundary uses ArcPy[13]. However, ArcPy is not open sourced. Upon submission, due to policy adjustments, the SURF_CLI_CHN_MUL_DAY dataset has just been closed for sharing (may reopen), we provide two options: (1) calculate time series using the archived SURF_CLI_CHN_MUL_DAY data if the researcher had (2) calculate time series using our released data; the principle is to calculate the overlapping areas of the given watershed and the watersheds we have

[4] https://rasterio.readthedocs.io/en/latest/

[5] https://shapely.readthedocs.io/en/stable/manual.html

[6] https://pyproj4.github.io/pyproj/stable/

[7] https://richdem.readthedocs.io/en/latest/

[8] https://unidata.github.io/netcdf4-python/

[9] http://xarray.pydata.org/en/stable/

[10] https://pypi.org/project/pyshp/

[11] https://gdal.org/api/python.html

[12] https://docs.python.org/3/library/multiprocessing.html

[13] https://pro.arcgis.com/zh-cn/pro-app/latest/arcpy/get-started/what-is-arcpy-.htm

calculated and then calculate the meteorological time series of the given watersheds by weighting, codes can be found in the GitHub repository. The GDBD dataset can be downloaded at https://www.cger.nies.go.jp/db/gdbd/gdbd_index_e.html. ASTER GDEM dataset can be downloaded at: https://asterweb.jpl.nasa.gov/gdem.asp. The GLHYMPS dataset can be downloaded at https://dataverse.scholarsportal.info/dataset.xhtml?persistentId=doi:10.5683/SP2/DLGXYO; MODIS MCD12Q1 can be obtained from https://lpdaac.usgs.gov/products/mcd12q1v006/; MODIS MCD15A3 can be obtained from https://lpdaac.usgs.gov/products/mcd15a3hv006/; soil hydraulic and thermal properties can be downloaded after registration: http://globalchange.bnu.edu.cn/research/soil5.jsp; soil property data can be downloaded after registration: http://globalchange.bnu.edu.cn/research/soil2; and SoilGrids250 m data download links: https://files.isric.org/soilgrids/former/2017-03-10/data/ with a list of descriptions: https://github.com/ISRICWorldSoil/SoilGrids250m/blob/master/grids/models/META_GEOTIFF_1B.csv.

Appendix E: Basin boundaries

This section briefly introduces how the basin boundaries are derived. The basin boundary data used in this research are obtained from the GBDB (Masutomi et al., 2009) dataset. The GDBD dataset first distinguishes sinks caused by DEM errors; then, stream burning (Maidment, 1996) and ridge fencing methods are used to modify the seeded DEM, and basin boundaries are produced with standardized procedures (Jenson and Domingue, 1988; Maidment and Morehouse, 2002). Then, the gauging station data from the GRDC dataset are used to calibrate the derived basin boundaries. The derived basin areas were compared with the observed basin areas, and they showed a high degree of consistency with the observed basin data.

Appendix F: Guidelines for calculating attributes for custom catchments

The published code[14] supports the automation of the calculation of the attributes for any given river basin and the generation of statistics files. In general, the user only needs to prepare the source data and ensure that the code environment is installed correctly, and then the user can run the code to calculate all attributes for the given river basin. The following describes the steps to generate data for any given watershed.

1. Prepare source data

In this step, the user needs to download the source data and place it in the cor-responding location (Table F1). The code supports the calculation of meteorological time series based on the SURF_CLI_CHN_MUL_DAY dataset. If the basin the user needs to calculate is not in China, then the user needs to format the collected meteorological time series into the same format as the time series generated by the code. A sample file is available in the GitHub library.

[14] https://github.com/haozhen315/CCAM-China-Catchment-Attributes-and-Meteorology-dataset

Table F1: Instructions for preparing data sources

Data source	Download link	Example	Note
ASTER GDEM	https://search.earthdata.nasa.gov/search/ https://www.jspacesystems.or.jp/ersdac/GDEM/E/	./data/dems/ *.tif	
GLHYMPS	https://dataverse.scholarsportal.info/dataset.xhtml?persistentId=doi:10.5683/SP2/DLGXYO (using source data requires merging multiple small pieces to a single TIFF) https://1drv.ms/u/s!AqzR0fLyn9KKspF6HAAuXU9Twkkz1Q?e=QCPFAm (our processed file) https://1drv.ms/u/s!AqzR0fLyn9KKspF70EPmDubS5V2qTQ?e=Rbybwa (our processed file)	./data/processed_permeability.tif ./data/processed_porosity.tif	
GLiM	https://csdms.colorado.edu/wiki/Data:GLiM https://1drv.ms/u/s!AqzR0fLyn9KKspF5Vktb-zlmd_Ctxg?e=G6fOuh (our processed file)	./data/processed_glim.py	
MCD12Q1	https://lpdaac.usgs.gov/products/mcd12q1v006/ https://1drv.ms/u/s!AqzR0fLyn9KKspF4xxbe0xM7qJN	./data/processed_igbp.tif	

	zkA?e=vyFcFj (our processed file)		
MCD15A3	https://lpdaac.usgs.gov/products/mcd15a3hv006/	./data/MCD15A3/MCD15A3H.A2002185.h22v04.006.2015149102803.hdf	
MOD13Q1	https://lpdaac.usgs.gov/products/mod13q1v006/	./data/MOD13Q1/MOD13Q1.A2002186.h22v04.006.2015149102803.hdf	
Soil	http://globalchange.bnu.edu.cn/research/soil5.jsp	./data/soil_souce_data/binary/log_k_s_l1	
Soil	https://files.isric.org/soilgrids/former/2017-03-10/data/	./data/soil_souce_data/tif/BDTICM_M_250m_ll.tif	Description: https://github.com/ISRICWorldSoil/SoilGrids250m/blob/master/grids/models/META_GEOTIFF_1B.csv
Soil	http://globalchange.bnu.edu.cn/research/soil2	./data/soil_souce_data/tif/SA.nc	
Root depth	https://github.com/haozhen315/CCAM-China-Catchment-Attributes-and-Meteorology-dataset/blob/main/data/root_depth_calculated.txt	./data/root_depth_calculated.txt	Calculated root depth of each land type according to (Zeng, 2001).
GLiM name mapping	https://github.com/haozhen315/CCAM-China-Catchment-Attributes-and-Meteorology-dataset/blob/main/data/glim_name_short_long.txt https://github.com/haozhen315/CCAM-China-Catchment-Attributes-and-Meteorology-	./data/glim_cate_number_mapping.csv ./data/glim_name_short_long.txt	These files are used for name conversions in the program.

	dataset/blob/main/data/glim_cate_number_mapping.csv		
GDBD	https://www.cger.nies.go.jp/db/gdbd/gdbd_index_e.html	./data/river_network/as_streams_wgs.shp	River network shapefiles are used to determine river basin shape factors. The source data need to be reprojected to EPSG:4326 (using ArcMap or QGIS) to successfully run the code. Note that files in different regions have different names.

485

2. Run the code

When all the data are ready, the user can run the code calculate_all_attributes.py to calculate all attributes or run separate scripts (e.g., soil.py) to calculate indicators for specific categories. The result will appear in the output folder.

Financial support

490 This research was supported by the National Key Research and Development Program (2018YFC0407901, 2018YFC0407905), the National Natural Science Fund of China (51779100), and the Central Public-interest Scientific Institution Basal Research Fund (HKY-JBYW-2020-21, HKY-JBYW-2020-07, HKY- JBYW-2021-02).

References

Abrams, M., Crippen, R., and Fujisada, H.: ASTER global digital elevation model (GDEM) and ASTER global water body dataset
495 (ASTWBD), Remote Sensing, 12, 1156, 2020.
Addor, N., Newman, A. J., Mizukami, N., and Clark, M. P.: The CAMELS data set: catchment attributes and meteorology for large-sample studies, Hydrology and Earth System Sciences (HESS), 21, 5293-5313, 2017.
Addor, N., Do, H. X., Alvarez-Garreton, C., Coxon, G., Fowler, K., and Mendoza, P. A.: Large-sample hydrology: recent progress, guidelines for new datasets and grand challenges, Hydrological Sciences Journal, 65, 712-725, 2020.
500 Alvarez-Garreton, C., Mendoza, P. A., Boisier, J. P., Addor, N., Galleguillos, M., Zambrano-Bigiarini, M., Lara, A., Cortes, G., Garreaud, R., and McPhee, J.: The CAMELS-CL dataset: catchment attributes and meteorology for large sample studies-Chile dataset, Hydrology and Earth System Sciences, 22, 5817-5846, 2018.
Belward, A. S., Estes, J. E., and Kline, K. D.: The IGBP-DIS global 1-km land-cover data set DISCover: A project overview, Photogrammetric Engineering and Remote Sensing, 65, 1013-1020, 1999.
505 Bureau of Geology and Mineral Resources of Xinjiang [BGX].: 'Geological map of Xinjiang Uygur, Autonomous Region, China, version 2, scale 1:1,500,000', 1992
Berghuijs, W. R., Aalbers, E. E., Larsen, J. R., Trancoso, R., and Woods, R. A.: Recent changes in extreme floods across multiple continents, Environmental Research Letters, 12, 114035, 2017.
Blume, T., van Meerveld, I., and Weiler, M.: Incentives for field hydrology and data sharing: collaboration and compensation: reply to "A
510 need for incentivizing field hydrology, especially in an era of open data", Hydrological Sciences Journal, 63, 1266-1268, 2018.
Brodeur, Z. P., Herman, J. D., and Steinschneider, S.: Bootstrap Aggregation and Cross-Validation Methods to Reduce Overfitting in Reservoir Control Policy Search, Water Resources Research, 56, e2020WR027184, 2020.
Buermann, W., Dong, J., Zeng, X., Myneni, R. B., and Dickinson, R. E.: Evaluation of the utility of satellite-based vegetation leaf area index data for climate simulations, Journal of Climate, 14, 3536-3550, 2001.

Ceola, S., Arheimer, B., Baratti, E., Blöschl, G., Capell, R., Castellarin, A., Freer, J., Han, D., Hrachowitz, M., and Hundecha, Y.: Virtual laboratories: new opportunities for collaborative water science, Hydrology Earth System Sciences, 19, 2101-2117, 2015.

Chagas, V. B., Chaffe, P. L., Addor, N., Fan, F. M., Fleischmann, A. S., Paiva, R. C., and Siqueira, V. A.: CAMELS-BR: hydrometeorological time series and landscape attributes for 897 catchments in Brazil, Earth System Science Data, 12, 2075-2096, 2020.

Coron, L., Andreassian, V., Perrin, C., Lerat, J., Vaze, J., Bourqui, M., and Hendrickx, F.: Crash testing hydrological models in contrasted climate conditions: An experiment on 216 Australian catchments, Water Resources Research, 48, 2012.

China Geological Survey [CGS].: '1:2,500,000-scale digital geological map database of China', 2001Coxon, G., Addor, N., Bloomfield, J. P., Freer, J., Fry, M., Hannaford, J., Howden, N. J., Lane, R., Lewis, M., and Robinson, E. L.: CAMELS-GB: hydrometeorological time series and landscape attributes for 671 catchments in Great Britain, Earth System Science Data, 12, 2459-2483, 2020.

Dai, Y., Xin, Q., Wei, N., Zhang, Y., Shangguan, W., Yuan, H., Zhang, S., Liu, S., and Lu, X.: A global high-resolution data set of soil hydraulic and thermal properties for land surface modeling, Journal of Advances in Modeling Earth Systems, 11, 2996-3023, 2019.

de Araújo, J. C. and González Piedra, J. I.: Comparative hydrology: analysis of a semiarid and a humid tropical watershed, Hydrological Processes: An International Journal, 23, 1169-1178, 2009.

Desborough, C. E.: The impact of root weighting on the response of transpiration to moisture stress in land surface schemes, Monthly Weather Review, 125, 1920-1930, 1997.

Didan, K.: MOD13A3 MODIS/Terra vegetation indices monthly L3 global 1km SIN grid V006 (Data set) NASA EOSDIS Land Process, 2015.

Feng, D., Fang, K., and Shen, C.: Enhancing streamflow forecast and extracting insights using long-short term memory networks with data integration at continental scales, Water Resources Research, 56, e2019WR026793, 2020.

Friedl, M. A., Sulla-Menashe, D., Tan, B., Schneider, A., Ramankutty, N., Sibley, A., and Huang, X.: MODIS Collection 5 global land cover: Algorithm refinements and characterization of new datasets, Remote sensing of Environment, 114, 168-182, 2010.

Gleeson, T., Moosdorf, N., Hartmann, J., and Van Beek, L.: A glimpse beneath earth's surface: GLobal HYdrogeology MaPS (GLHYMPS) of permeability and porosity, Geophysical Research Letters, 41, 3891-3898, 2014.

Gleeson, T., Smith, L., Moosdorf, N., Hartmann, J., Dürr, H. H., Manning, A. H., van Beek, L. P., and Jellinek, A. M.: Mapping permeability over the surface of the Earth, Geophysical Research Letters, 38, 2011.

Gudmundsson, L., Leonard, M., Do, H. X., Westra, S., and Seneviratne, S. I.: Observed trends in global indicators of mean and extreme streamflow, Geophysical Research Letters, 46, 756-766, 2019.

Hartmann, J. and Moosdorf, N.: The new global lithological map database GLiM: A representation of rock properties at the Earth surface, Geochemistry, Geophysics, Geosystems, 13, 2012.

Hengl, T., Mendes de Jesus, J., Heuvelink, G. B., Ruiperez Gonzalez, M., Kilibarda, M., Blagotić, A., Shangguan, W., Wright, M. N., Geng, X., and Bauer-Marschallinger, B.: SoilGrids250m: Global gridded soil information based on machine learning, PLoS one, 12, e0169748, 2017.

Horn, B. K.: Hill shading and the reflectance map, Proceedings of the IEEE, 69, 14-47, 1981.

Huang, H., Han, Y., Cao, M., Song, J., and Xiao, H.: Spatial-temporal variation of aridity index of China during 1960–2013, Advances in Meteorology, 2016, 2016.

Jenson, S. K. and Domingue, J. O.: Extracting topographic structure from digital elevation data for geographic information system analysis, Photogrammetric engineering remote sensing, 54, 1593-1600, 1988.

Kendall, M. G.: A new measure of rank correlation, Biometrika, 30, 81-93, 1938.

Knoben, W. J., Freer, J. E., and Woods, R. A.: Inherent benchmark or not? Comparing Nash–Sutcliffe and Kling–Gupta efficiency scores, Hydrology and Earth System Sciences, 23, 4323-4331, 2019.

Knyazikhin, Y.: MODIS leaf area index (LAI) and fraction of photosynthetically active radiation absorbed by vegetation (FPAR) product (MOD 15) algorithm theoretical basis document, http://eospso. gsfc. nasa. gov/atbd/modistabls. heml, 1999.

Kollat, J., Reed, P., and Wagener, T.: When are multiobjective calibration trade-offs in hydrologic models meaningful?, Water Resources Research, 48, 2012a.

Kollat, J., Reed, P., and Wagener, T. J. W. R. R.: When are multiobjective calibration trade-offs in hydrologic models meaningful?, 48, 2012b.

Kratzert, F., Klotz, D., Shalev, G., Klambauer, G., Hochreiter, S., and Nearing, G.: Towards learning universal, regional, and local hydrological behaviors via machine learning applied to large-sample datasets, Hydrology & Earth System Sciences, 23, 2019.

Lane, R. A., Coxon, G., Freer, J. E., Wagener, T., Johnes, P. J., Bloomfield, J. P., Greene, S., Macleod, C. J., and Reaney, S. M.: Benchmarking the predictive capability of hydrological models for river flow and flood peak predictions across over 1000 catchments in Great Britain, Hydrology and Earth System Sciences, 23, 4011-4032, 2019.

Legasa, M. and Gutiérrez, J. M.: Multisite Weather Generators using Bayesian Networks: An illustrative case study for precipitation occurrence, Water Resources Research, 56, e2019WR026416, 2020.

Lehner, B.: HydroBASINS: Global watershed boundaries and sub-basin delineations derived from HydroSHEDS data at 15 second resolution—Technical documentation version 1. c, 2014.

Lehner, B., Liermann, C. R., Revenga, C., Vörösmarty, C., Fekete, B., Crouzet, P., Döll, P., Endejan, M., Frenken, K., and Magome, J.: Global reservoir and dam (grand) database, Technical Documentation, Version, 1, 1-14, 2011.
Linke, S., Lehner, B., Dallaire, C. O., Ariwi, J., Grill, G., Anand, M., Beames, P., Burchard-Levine, V., Maxwell, S., and Moidu, H.: Global hydro-environmental sub-basin and river reach characteristics at high spatial resolution, Scientific data, 6, 1-15, 2019.
Liu, B., Xu, M., Henderson, M., and Gong, W.: A spatial analysis of pan evaporation trends in China, 1955–2000, Journal of Geophysical Research: Atmospheres, 109, 2004.
Liu, Q., Yang, Z., and Xia, X.: Trends for pan evaporation during 1959-2000 in China, Procedia Environmental Sciences, 2, 1934-1941, 2010.
Liu, Y., Zheng, J., Hao, Z., and Zhang, X.: Unprecedented warming revealed from multi-proxy reconstruction of temperature in southern China for the past 160 years, Advances in Atmospheric Sciences, 34, 977-982, 2017.
Maidment, D. R.: GIS and hydrologic modeling-an assessment of progress, Third International Conference on GIS and Environmental Modeling, Santa Fe, New Mexico,
Maidment, D. R. and Morehouse, S.: Arc Hydro: GIS for water resources, ESRI, Inc.2002.
Masutomi, Y., Inui, Y., Takahashi, K., and Matsuoka, Y.: Development of highly accurate global polygonal drainage basin data, Hydrological Processes: An International Journal, 23, 572-584, 2009.
Ministry of Geology and Mineral Resources of the People's Republic of China [MGC].: 'Geological map of Nei Mongol Autonomous Region, People's Republic of China, scale 1:1,500,000', 1991Mei, Y., Maggioni, V., Houser, P., Xue, Y., and Rouf, T.: A nonparametric statistical technique for spatial downscaling of precipitation over High Mountain Asia, Water Resources Research, 56, e2020WR027472, 2020.
Myneni, R., Knyazikhin, Y., and Park, T.: MOD15A2H MODIS/terra leaf area index/FPAR 8-day L4 global 500 m SIN grid V006, NASA EOSDIS Land Processes DAAC, 2015.
Nevo, S., Anisimov, V., Elidan, G., El-Yaniv, R., Giencke, P., Gigi, Y., Hassidim, A., Moshe, Z., Schlesinger, M., and Shalev, G.: ML for flood forecasting at scale, arXiv preprint arXiv:1901.09583, 2019.
Newman, A., Clark, M., Sampson, K., Wood, A., Hay, L., Bock, A., Viger, R., Blodgett, D., Brekke, L., and Arnold, J.: Development of a large-sample watershed-scale hydrometeorological data set for the contiguous USA: data set characteristics and assessment of regional variability in hydrologic model performance, Hydrology and Earth System Sciences, 19, 209-223, 2015.
Ni, H. and Benson, S. M.: Using Unsupervised Machine Learning to Characterize Capillary Flow and Residual Trapping, Water Resources Research, 56, e2020WR027473, 2020.
Oudin, L., Andréassian, V., Lerat, J., and Michel, C.: Has land cover a significant impact on mean annual streamflow? An international assessment using 1508 catchments, Journal of hydrology, 357, 303-316, 2008.
Running, S., Mu, Q., and Zhao, M.: MOD16A2 MODIS/Terra Net Evapotranspiration 8-Day L4 Global 500 m SIN Grid V006. NASA EOSDIS Land Processes DAAC, 2017.
Seybold, H., Rothman, D. H., and Kirchner, J. W.: Climate's watermark in the geometry of stream networks, Geophysical Research Letters, 44, 2272-2280, 2017.
Shangguan, W., Dai, Y., Duan, Q., Liu, B., and Yuan, H.: A global soil data set for earth system modeling, Journal of Advances in Modeling Earth Systems, 6, 249-263, 2014.
Shangguan, W., Dai, Y., Liu, B., Zhu, A., Duan, Q., Wu, L., Ji, D., Ye, A., Yuan, H., and Zhang, Q.: A China data set of soil properties for land surface modeling, Journal of Advances in Modeling Earth Systems, 5, 212-224, 2013.
Shen, C., Laloy, E., Elshorbagy, A., Albert, A., Bales, J., Chang, F.-J., Ganguly, S., Hsu, K.-L., Kifer, D., and Fang, Z.: HESS Opinions: Incubating deep-learning-powered hydrologic science advances as a community, Hydrology and Earth System Sciences (Online), 22, 2018.
Silberstein, R.: Hydrological models are so good, do we still need data?, Environmental Modelling & Software, 21, 1340-1352, 2006.
Singh, R., Archfield, S., and Wagener, T.: Identifying dominant controls on hydrologic parameter transfer from gauged to ungauged catchments–A comparative hydrology approach, Journal of Hydrology, 517, 985-996, 2014a.
Singh, R., van Werkhoven, K., and Wagener, T.: Hydrological impacts of climate change in gauged and ungauged watersheds of the Olifants basin: a trading-space-for-time approach, Hydrological Sciences Journal, 59, 29-55, 2014b.
Subramanya, K.: Engineering Hydrology, 4e, Tata McGraw-Hill Education2013.
Sulla-Menashe, D. and Friedl, M. A.: User guide to collection 6 MODIS land cover (MCD12Q1 and MCD12C1) product, USGS: Reston, VA, USA, 1-18, 2018.
Tyralis, H., Papacharalampous, G., and Tantanee, S.: How to explain and predict the shape parameter of the generalized extreme value distribution of streamflow extremes using a big dataset, Journal of Hydrology, 574, 628-645, 2019.
van Werkhoven, K., Wagener, T., Reed, P., and Tang, Y. J. W. R. R.: Characterization of watershed model behavior across a hydroclimatic gradient, 44, 2008.
van Wijk, M. T. and Williams, M.: Optical instruments for measuring leaf area index in low vegetation: application in arctic ecosystems, Ecological Applications, 15, 1462-1470, 2005.
Voepel, H., Ruddell, B., Schumer, R., Troch, P. A., Brooks, P. D., Neal, A., Durcik, M., and Sivapalan, M.: Quantifying the role of climate and landscape characteristics on hydrologic partitioning and vegetation response, Water Resources Research, 47, 2011.

Wang, J., Chen, M., Lü, G., Yue, S., Wen, Y., Lan, Z., and Zhang, S.: A data sharing method in the open web environment: Data sharing in hydrology, Journal of Hydrology, 587, 124973, 2020.
Wickel, B., Lehner, B., and Sindorf, N.: HydroSHEDS: A global comprehensive hydrographic dataset, AGU Fall Meeting Abstracts, H11H-05,
Wongso, E., Nateghi, R., Zaitchik, B., Quiring, S., and Kumar, R.: A Data-Driven Framework to Characterize State-Level Water Use in the United States, Water Resources Research, 56, e2019WR024894, 2020.
Woods, R. A.: Analytical model of seasonal climate impacts on snow hydrology: Continuous snowpacks, Advances in Water Resources, 32, 1465-1481, 2009.
Xu, Y., Gao, X., Shen, Y., Xu, C., Shi, Y., and Giorgi, a.: A daily temperature dataset over China and its application in validating a RCM simulation, Advances in Atmospheric sciences, 26, 763-772, 2009.
Yamazaki, D., Ikeshima, D., Sosa, J., Bates, P. D., Allen, G. H., and Pavelsky, T. M.: MERIT Hydro: a high-resolution global hydrography map based on latest topography dataset, Water Resources Research, 55, 5053-5073, 2019.
Zeng, X.: Global vegetation root distribution for land modeling, Journal of Hydrometeorology, 2, 525-530, 2001.